LBL-3986
c.1

OPTIMIZATION OF STRENGTH AND DUCTILITY IN Fe-Mn TRIP STEELS

Glenn Thomas Haddick
(M. S. thesis)

June 1976

Prepared for the U. S. Energy Research and Development Administration under Contract W-7405-ENG-48

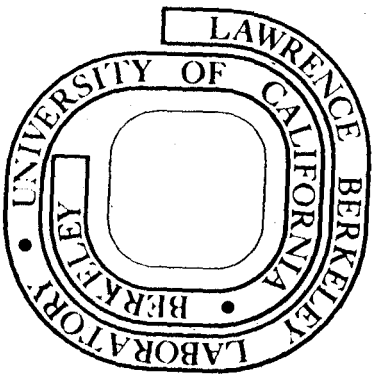

LBL-3986
c.1

DISCLAIMER

Table of Contents

OPTIMIZATION OF STRENGTH AND DUCTILITY IN Fe-Mn TRIP STEELS

Glenn Thomas Haddick

Materials and Molecular Research Division, Lawrence Berkeley Laboratory
and Department of Materials Science and Engineering,
University of California, Berkeley, California 94720

ABSTRACT

A series of Fe-Mn alloys containing 16-20% Mn, 0-0.15% C, and 0-1.0% Mo were designed to illustrate the effect of balanced chemistry and heat treatment for the optimization of the mechanical properties of a class of steels known as TRIP steels. The mechanical properties of TRIP steels in a room temperature test depends on the position of the M_s and M_d temperatures, which are controlled by the chemical composition, with respect to room temperature. In general, the strength and ductility of the 16% Mn steels improved with increasing alloy content while the 20% Mn alloys were less sensitive to increased alloy content.

As the chemical composition was increased, the phase composition tended toward more ε martensite. This increase in the ε martensite content indicated that the M_d temperature was decreasing towards room temperature, and the effect of the decreasing M_d temperature showed itself in the variation of the mechanical properties. The 16% Mn alloy showed a 30 ksi yield strength and 30% elongation while the 16% Mn - 0.08% C - 1.0% Mo alloy had a 46 ksi yield strength and 46% elongation. Thermal cycling was used to increase the ε martensite content further

to increase the strength and ductility. The 16% Mn-0.08% C-1.0% Mo alloy after thermal cycling had a 60 ksi yield strength and 53% elongation. The ductile-brittle transition temperature (DBTT) of these alloys were also controlled by the chemical composition. The 16% Mn alloy had a DBTT of -160°C while the 16% Mo-0.13% C alloy had a DBTT of -80°C. The addition of a carbide forming element and the reduction of carbon caused the DBTT to decrease. The 16% Mn-0.08% C-1.0% Mo alloy had a DBTT of -140°C.

I. INTRODUCTION

Alloy design has been an important aspect of materials research for many years,[1,2] and the goal that alloy design seeks to fulfill is a liaison between the pure science of materials research and the final application of the science in engineering, manufacturing and construction. This investigation shows the connection between a background of scientific knowledge in a class of steels known as TRIP steels, and the goal of developing a particular TRIP steel for application in cost effective products which require high uniform elongation and notch toughness. Two examples of products that require these properties are gas and oil pipelines and energy absorbing devices.[3] When one thinks of TRIP steels, the thought of the Cr-Ni TRIP steels springs to mind.[4-15] However, most common structures do not require the high strengths attained by the Cr-Ni steels, nor is their corrosion resistance necessary. Clearly, there is a wide range of low and medium strength steels of lower initial cost than the Cr-Ni TRIP steels, that should be developed to fill the needs that have been mentioned. For this purpose a series of Fe-Mn, Fe-Mn-C and Fe-Mn-Mo-C steels were designed to meet the specifications of steels now being used in industrial projects (e.g. the Alaskan oil pipeline) that would possess better uniform elongation and impact toughness.[16]

High strength steels had always been plagued with limited elongation,[1] and the quest became one of designing a high strength steel that possessed high elongations. One mechanism that was known to increase the uniform elongation was the strain induced γ (gamma) to α'(alpha)

transformation in metastable austenitic steels.[17] In addition, thermo-mechanical treatments similar to ausforming were used to increase the dislocation density in the steels.[3] The resulting properties of these steels (i.e. TRIP steels) were characterized by high yield and ultimate strengths due to the high dislocation density and by high elongations due to transformation strengthening during straining. In the present investigation, the goal was not to improve the properties of pre-existing steels that have specialized applications, but to optimize the mechanical properties of a whole family of steels suitable for broader applications. A recent investigation of Fe-Mn binary alloys[18] indicated that the 16 and 20% Mn alloys had the required transformation characteristics of a TRIP steel. These two compositions formed the basis of the present design effort.

A knowledge of the variation of the mechanical properties with chemical composition and test temperature is necessary to understand the secrets hidden in any TRIP steel investigation. Figure 1 shows the variation of mechanical properties - yield strength, ultimate strength, and percent elongation - versus test temperature after Tamura et al.[19] who studied annealed Fe-Ni, Fe-Cr-Ni and Fe-Mn-C alloys. The M_s and M_d temperatures are determined by the chemical composition which further determines the location of room temperature with respect to the M_s and M_d temperatures. The thrust of this diagram is that the chemical composition determines the optimum percent elongation attainable in a room temperature test. Hidden from the diagram is the effect of the microstructure and carbide forming elements on the mechanical properties.

The effect of the microstructure varies from system to system, but the effect of carbide forming elements has the following influence. Carbide forming elements deplete localized volumes of the steel of carbon which raises the M_s temperature making the steel mechanically less stable. The details of this process are not well understood, but it has been observed that the addition of carbide forming elements to TRIP steels has the effect of increasing the strain hardening rate and the elongation.[20,21] The addition of carbide forming elements lowers the stacking fault energy of austenite.[22]

Schanfein's investigation[18] of Fe-Mn binary alloys showed that the microstructures produced on quenching and refrigerating the alloys to -196°C varied systematically with increasing Mn content as shown in Fig. 2. This diagram shows that compositions containing 16 and 20% Mn have M_s temperatures in the vicinity of room temperature. Therefore, the mechanical properties of the 16 and 20% Mn alloys would be expected to increase with additions of C and Mo which depress the M_s and M_d temperatures (see Fig. 1). Now, however, one more variable enters the picture, vis the Fe-Mn alloys have an intermediate ε-martensite phase which drastically alters the microstructure. The effect of this altered microstructure must be determined with respect to the predictions that have been made about mechanical properties and chemical composition. One of the premier studies of the variation of microstructure with heat treatment of Fe-Mn steels was done by Gordon-Parr[23] who chose an 18.5% Mn alloy for investigation. Schumann[24,25] and Holden et al[26] have also done thorough studies of the variation of microstructure and mechanical properties in Fe-Mn alloys. In general, austenitizing and quenching

an alloy in the composition range of the present investigation produces a mixed microstructure of γ, ε and α', while air cooling a similar alloy produces a microstructure of γ and ε. The effects of ε on the mechanical properties of Fe-Mn steels cannot be understated, particularly when combined with the fact that carbide forming elements lower the stacking fault energy of austenite. The limiting feature of the microstructure in Fe-Mn steels was the cleavage of ε near grain boundaries,

This investigation started with Fe- 16 and 20% Mn binary alloys which were known to have mechanically induced phase transformations. Additions of C and Mo were made to decrease the M_s and M_d temperatures — to increase the strength and ductility of the alloys, and a thermal cycling heat treatment was designed to anneal the transformation stresses caused by the transformation to ε-martensite.[24]

II. EXPERIMENTAL PROCEDURES

A. Alloy Preparation

The alloys used in this investigation were prepared in a Temescal 125 kV vacuum induction furnace. The elements used were high purity (99.9+%) iron, manganese, molybdenum, carbon, titanium and aluminum, and were melted in magnesium oxide crucibles in an argon atmosphere. The alloy compositions and the numerology used throughout this paper are listed in Table I. After melting, twenty pound ingots were cast in copper chill molds and furnace cooled in the argon atmosphere. Homogenization was consumated at 1200°C for twenty-four hours in an argon atmosphere, and then the ingots were furnace cooled. The homogenized ingots were next upset and crossforged at 1200°C in air to a cross-section of 2 3/4 in. wide by 1/2 in. thick followed by air cooling. The carbon free alloys contained 0.15% titanium and 0.10% aluminum to scavenge interstitials, while the carbon containing alloys contained 0.10% aluminum to inactivate nitrogen and oxygen interstitials.

B. Heat Treatment

After forging, the bars were cut into blanks, 2 1/2 in. and 3 in. long, and were austenitized at 900°C for two hours in air followed by agitated quenching in an ice brine bath (-10°C) and then refrigerated in liquid nitrogen (-196°C). A material processing diagram is shown in Fig. 3.

A thermal cycling heat treatment was performed on tensile specimens of the 16% and 20% manganese alloys. A schematic of the heat treatment is shown in Fig. 4, while a dilatometric phase diagram is shown in Fig. 2 to delineate the effects of the heat treatment. The high temperature portion of the thermal cycling treatments were accomplished in air and the low temperature portion of the treatments were done in an ice water bath followed by refrigeration to liquid nitrogen. The specimens were then blown dry to bring their temperature back up to room temperature.

C. Specimen Preparation

After austenitization and quenching the 2 1/2 in. long blanks were machined into Charpy bars according to ASTM specification E23-72 with the specimen dimensions as shown in Fig. 5a. Tensile specimens were machined from the 3 in. blanks according to ASTM specification E8-69 as shown in Fig. 5b. Both the Charpy bars and the tensile specimens were carefully machined and finish ground to minimize any mechanically induced phase transformations.

D. Mechanical Testing

1. Hardness Testing

Hardness tests were performed on all as heat treated alloys and on small cuboid specimens used to follow the changes in mechanical properties during thermal cycling (see Fig. 3). The Rockwell "C" scale was used and five readings were used for each data point. The various hardness values obtained are shown in Table II.

2. Charpy Testing

Charpy tests were performed on a 223 ft-lb capacity impact testing machine according to ASTM specification E23-72. Data points at room, dry ice, and liquid nitrogen temperatures were established with two tests while intermediate temperature data points were established using one test. The various temperature baths were made from mixtures of methanol and dry ice, corresponding to a temperature range of 0 to -78°C, and isopentane and liquid nitrogen, corresponding to a range in temperatures of -80 to -150°C.

3. Tensile Testing

Tensile tests were carried out on a 5000 kg capacity Instron testing machine at a crosshead speed of 0.1 cm/min. at room temperature. The 0.2% offset method of determining the yield stress was used. Two specimens of each composition were broken to determine each data point. Elongations were measured from the specimen using a traveling microscope. Tables III and IV show tensile data for the as heat treated specimens and the thermal cycled specimens respectively.

E. Microscopy

1. Optical Metallography

Specimens were prepared for optical metallography by first cutting a cube of material from an unused charpy bar on a diamond wheel cutting machine. The cubes were then mounted in a cold setting resin and ground on 0, 00, and 000 aluminum oxide emery papers followed by ultrasonic cleaning in alcohol. The specimens were then mechanically polished on 6 and 1μ (micron) diamond paste wheels lubricated with kerosene,

followed by ultrasonic cleaning again. Next, specimens were electro-polished in a solution containing 75g CrO_3 powder + 400 ml glacial acetic acid + 20 ml distilled water at from 10 to 12°C and at various voltages depending on the alloy composition. A two minute polishing period was usually sufficient to remove the scratches from the previous step.

Etching was accomplished using Klemm's reagent which contains 50 ml cold saturated sodium bisulphate ($Na_2S_2O_3$) in distilled water and 5g potasium meta-bisulphite ($K_2S_2O_5$). Klemm's reagent distinguishes between austenite and epsilon martensite (brown and white respectively) and alpha martensite (black with more surface relief than the previous two phases). Specimens were etched from thirty seconds to one minute to produce a readily observable surface.

Pictures were taken on a Carl Zeiss Ultraphot II microscope at 200X and 500X using the Nomarski interference contrast optics because of the overall low surface relief. Polaroid P/N type 55 film was used and prints were made to improve contrast.

2. Scanning Electron Microscopy

The fracture surfaces of broken Charpy bars were examined on a Jeolco JSM-U3 and an AMR 1000 scanning electron microscope operated at 25 kV. Micrographs were taken at magnifications of 200, 300, and 1000.

F. X-Ray Diffraction Analysis

Specimens for x-ray analysis were prepared in the same manner as the optical metallography specimens except that etching was omitted. Scans were made on a Picker x-ray diffractometer using copper K-alpha

radiation with an LiF monochromator between the diffracted beam and the detector. Scans were run at two degrees per minute, and a two degree slit was employed. Quantitative phase measurements were made by comparing the integrated intensities of the $(200)_\alpha$, $(211)_\alpha$, $(01.2)_\varepsilon$, $(01.3)_\varepsilon$ and $(220)_\gamma$ peaks. Calculations based on the four combinations of peaks were averaged together for each alloy tested. Phase determinations made on broken tensile specimens were handled using the $(110)_\alpha$, $(01.1)_\varepsilon$, and $(111)_\gamma$ peaks. Because of the small area of the broken tensile specimens, higher angle peaks were not visible. Table V shows the phase compositions of the alloys after the initial heat treatment, while Table VI shows the phase composition after tensile deformation.

G. Point Counting

Phase analysis by point counting using optical micrographs was used to varify the results from the x-ray phase analysis, and to confirm the trends of the phase composition with chemical composition. One hundred points on each of two photographs were used to establish the phase composition of the alloys, and Tables VI and VII are composites of both the x-ray and point counting techniques. The two phase analysis techniques were averaged because of the complicated microstructure, and the approximate nature of the x-ray method in these alloys.

III. EXPERIMENTAL RESULTS AND DISCUSSION

A. 16% Mn Microstructures

The microstructures of the 16% Mn steels are shown in Fig. 6, and the approximate phase analysis is shown in Table V. Several aspects of the microstructures are noteworthy, and the following observations are due entirely to the effectiveness of Klemm's reagent in developing the subtleties of the microstructures.

There has been some controversy over the sequence of the transformation from γ to either ε or α martensite. Much of this controversy has been over the sequence in Fe-Ni-Cr alloys,[27] but only to a limited extent in Fe-Mn-C alloys. Suemune and Ooka[28] used transmission electron microscopy on a series of Fe-Mn binary alloys, and concluded that the ε phase was a consequence of the formation of α martensite, and thus agreeing with Dash and Otte.[29] There have been other papers supporting the γ-ε-α transformation sequence in Fe-Mn alloys,[23,25,26,30] where the ε phase appears to be a transitional phase.

Figure 7 is an enlargement of Fig. 6a which corresponds to the 16-00 alloy and has 25%α, 47%ε, and 28%γ. At 'A' in Fig. 7, two α martensite lenses are present in an ε martensite plate, and at 'B' in the figure, α martensite is present in a region of γ. Gordon Parr[30] found the orientation relationship to be the Nishiyama relationship, and Schumann[25] found that the γ to α transformation had a 2.7% volume increase while the γ to ε transformation had a 2.1% volume decrease.

Figure 6b,c and d show the 16-05, 16-13, and 16-08-05 alloys respectively. These alloys contain less and less α in favor of ϵ which among other things gives a clearer representation of the original γ grain boundaries. These microstructural features will be shown to be very important in interpreting the mechanical properties, which in particular relate to the presence of ϵ martensite.

B. The Effect of Composition on the Tensile Properties of the 16% Mn Alloys

The variation of strengths versus carbon content is shown in Fig. 8 where yield and ultimate strengths are plotted for the 16 and 20% Mn alloys. The yield strength of the 16-00 alloy was substantially lower than either the 16-05 of the 16-13 alloys. Not only was the increase in yield strength due to the increased C content, but the M_s and M_d temperatures were lowered because of the increase in carbon. Specific information in the M_s and M_d temperatures was not obtained, however it is text book knowledge that an increase in carbon content produces a decrease in both the M_s and M_d. Thus, the M_d temperature moves closer to room temperature which means that there will be a greater proportion of strain induced transformation in the alloys with carbon, rather than a stress induced transformation. A stress induced transformation occurs when the testing temperature is so close to the M_s temperature that only a small stress below the plastic deformation stress is required to cause the transformation. This results in elongating the specimen without strain hardening. A strain induced transformation, as the name implies, occurs after plastic deformation has started. Thus, materials having only the strain induced transformation

will possess higher yield strengths than materials that deform via a stress induced transformation. This behavior can also be qualitatively determined from stress-strain curves.

The schematic stress-strain curves shown in Fig. 9 demonstrate the difference between the effect of stress and strain induced transformations on the appearance of the stress-strain curves. The 16-05 alloy which exhibited the stress induced transformation, showed no discontinuities in the stress-strain curve while the 16-13 alloy which exhibited the strain induced transformation showed large widely spaced discontinuities in its stress-strain curve. The 20-15 alloy also shown in the Fig. 9 exhibited the strain induced transformation but the difference between the 16-13 and 20-15 alloys was that the 20-15 alloy had a more stable austenitic microstructure, which produced the change in the yield point. More will be said about the 20% Mn alloys in a later section.

The variation of percent elongation and percent reduction of area for the 16-00, 16-05, and 16-13 alloys is shown in Fig. 10. Smooth curves were drawn through the data points and therefore the curves do not represent the absolute performance of the materials. However, it is seen from either the figure or the tabulated values that the elongation rises to a maximum at the 0.05% C level before dropping to the 0.13% C value. The variation of the reduction of area shows an analogous but much more abrupt behavior. From knowledge gained in previous TRIP steel projects,[8,9,12] it would be expected that the addition of carbon would slow the transformation to α with strain and improve the

elongation because of the depressed M_s temperature. Here we see the opposite effect which may be explained by the initial heat treatment and phase composition. The initial austenitization and quench trapped carbon in solution, and the 16-13 alloy had 67% ε martensite in the microstructure before deformation. The γ to ε transformation also has a 2.1% volume decrease. Carbon trapped in a predominantly ε martensite microstructure makes the 16-13 alloy brittle and in fact the scanning electron fractograph of the tensile specimen shows that fracture was taking place along ε-martensite plates. (see Fig. 11).

The variation of yield strength and tensile strength for the 16-08-05 and the 16-08-10 alloys is shown in Fig. 12. Note that the values on the zero percent molybdenum ordinate were obtained by interpolating values from the graph of tensile properties of the "plain carbon" alloys in Fig. 8. It is seen from Fig. 12 that the yield strength dropped when molybdenum was added to the Fe-Mn-C steels, and the microstructures indicate that the drop in the yield strength was a function of the grain size (see Fig. 6d). But, more important was the effect of molybdenum on the elongation shown in Fig. 13. The 16-08-10 alloy showed an elongation of 46% which was the greatest elongation observed for any of the 16% Mn alloys in the as quenched condition. The addition of molybdenum, a carbide forming element, to TRIP steels does two things. First, the carbide forming element locally decreases the carbon concentration by the formation of carbide particles, and second, carbide forming elements have been found to decrease the stacking fault energy.[22] These two factors have the opposite effects on the mechanical stability of austenite,[20] but their combined effect has been

to reduce the strain hardening rate to a level between that of the 16-05 and 16-13 alloys.

C. The Effect of Composition on the Ductile-Brittle Transition Temperature of the 16% Mn Alloys

Figure 14 shows the ductile-brittle transition temperature curves for all of the 16% Mn alloys. The 16-00 and 16-05 alloys possess what might be termed as the inherent Charpy V-notch properties of the 16% Mn alloys. Both alloys fractured by dimple rupture at room temperature and by quasi-cleavage at liquid nitrogen temperature (Fig. 15a and b respectively). Comparing Figs. 15a and 6a shows that the quasi-cleavage fracture surface follows the microstructural features of the alloy; thin rectangular shapes and flat surfaces correspond to areas where the fracture has traced out the ε martensite bands. Figure 15b also shows particles in the fracture surface, and by using an Energy Dispersive Analysis of X-rays (EDAX) unit, these particles were determined to be rich in titanium and others rich in magnesium. Figure 16 shows the EDAX analysis. The white dots in Fig. 16 indicate the analysis of the matrix material which as expected was rich in iron and manganese, while the grey lines indicate the analysis of the particle which was rich in titanium (the two vertical white lines show the K_α and the K_β position of titanium). This analysis demonstrates that the source of the dimple rupture fracture surface was partially due to titanium particles presumably due to the use of titanium as a gettering agent of interstitials, and partially due to magnesium particles presumably from the MgO crucibles used in preparing the ingots.

The performance of the 16-13 alloy fell dramatically from the level established by the previous two alloys. Not only did the impact energies fall 30 to 40 foot-pounds at each end of the temperature range, but the ductile-brittle transition temperature rose 80 to 90°C. Again, the scanning electron fractographs show that the fracture surface of the bar broken at -196°C had good dimensional agreement with the micrograph of the alloy (compare Fig. 15d with 6c). An electron microprobe analysis indicated that there was no chemical segregation of iron or manganese in the specimen, and the apparent reason for the grain boundary cleavage was the increase in the volume fraction of ε martensite in this alloy as compared with either the 16-00 or 16-05 alloy. It might be concluded that the 16% Mn alloys have a fracture mode transition at -196°C with increasing carbon content.

A similar fracture transition with increasing carbon content has been reported by Gerberich et al[11] where K_{Ic} specimens made from a high strength TRIP steel (9% Cr, 8% Ni, 4% Mo, plus C, Mn and Si) were found to fail by ductile fracture below 0.24% C and by cleavage above 0.27% C both at -196°C. The mode of failure was explained as cleavage of transformed martensite in the case of the 0.27% C alloys. The level of carbon needed to cause cleavage in the alloys of the present investigation seems to key on the ε martensite phase presumably because of the 2.1% volume decrease between γ and ε, and because of the high volume percent of ε martensite.

By adding only 0.08% C and either 0.5% or 1.0% Mo instead of 0.13% C to the 16% Mn binary alloy, the ductile-brittle transition

temperatures of these 16-08-05 and 16-08-10 alloys were lowered 60 to 80°C over the DBTT of the 16-13 alloy. There are two reasons that explain the observed behavior. First, the carbon content was lowered, which reduced the mechanical stability of the austenite. Second, the addition of a carbide forming element further reduced the carbon content in localized areas. Both factors allowed a greater amount of transformation which was qualitatively confirmed by hand magnet measurements. The qualitative magnetic measurements indicate the amount of α martensite and thus the ultimate amount of transformation since the ε martensite is non-magnetic. The fractographs of the 16-08-10 alloy (Fig. 17) showed that there was more quasi-cleavage in the liquid nitrogen test than exhibited by the 16-13 alloy while the room temperature test showed larger dimples in the rupture mode.

D. The Effect of Thermal Cycling on the Tensile Properties of the 16% Mn Alloys

Thermal cycling did several things to the microstructures and the mechanical properties of the 16% Mn alloys. But before much can be said about the properties, it must be ascertained what thermal cycling is and how it can be used to advantage in the design of alloys. After this has been accomplished, discussions concerning the changes in the mechanical properties due to the treatments can be made.

Figure 4 shows a schematic of the temperature time history given to the thermally cycled specimens. It should be added to the description already given in the section on experimental procedure that the high temperature steps were maintained for 15 minutes while the low temperature steps were kept for 5 minutes. The following table

compares the phase composition of two alloys in the as quenched and in the thermal cycled condition, after two complete cycles.

Alloy No	Phase Composition					
	As Quenched			Thermal Cycled		
	V_α	V_ε	V_γ	V_α	V_ε	V_γ
16-05	10	55	35	3	81	16
16-08-05	5	66	29	1	88	12

The x-ray data shows that the ε martensite phase increased at the expense of the α martensite and the γ. Gordon Parr[23] found similar results in an 18.5% Mn binary alloy which was quenched and then tempered at 450°C. Schumann and Heider[24] found that the thermal cycling treatment lowered the M_s temperature of a 16% Mn alloy for further transformation to ε martensite. Thus, thermal cycling prepared the microstructure to undergo a more complete transformation during deformation than the as quenched specimens, and since the M_d temperature was lowered, higher strengths should be obtained in the thermal cycled condition.

The results of thermal cycling on the mechanical properties of the 16% Mn alloys are shown in Table IV and in Figs. 8, 10, 12 and 13. In all instances, thermal cycling increased the yield strengths of the alloys, and a nominal increase in the ultimate strength was also noted. However, the most pronounced increases in the properties occured for the percent elongation and percent reduction of area. The 16-13 alloy for example that had showed relatively brittle behavior in the as quenched condition (28% elongation and 20% reduction of area), showed tremendous improvements after thermal cycling (40% elongation and 54% reduction

of area). The best combination of properties was obtained with the 16-08-10 alloy which exhibited 61 ksi yield strength, 156 ksi ultimate strength, 53% elongation, and 56% reduction of area. Remember that the 16-08-10 alloy had a ductile-brittle transition temperature well below that of the 16-13 alloy. Finally, to see how much improvement has been made, compare the figures of the 16-08-10 alloy with the 16-00 alloy which showed 30 ksi yield strength, 101 ksi ultimate strength, 30% elongation, and 71% reduction of area keeping in mind the goals of the investigation.

E. The Microstructures of the 20% Mn Alloys

The microstructures of the 20% Mn alloys are shown in Fig. 18. The micrographs show the distribution of the ε martensite in the materials while Table V shows the point counting and x-ray diffraction analysis of the alloys. When comparing the microstructures of the 20% Mn alloys to the microstructures of the 16% Mn alloys, two things become noticable. First, the morphology of the 20% Mn alloys did not change as much as the morphology of the 16% Mn alloys. As the alloy content of the 16% Mn alloys was increased, Figs. 6a through 6d, the morphology changed from a small broken-up structure to one that emphasized long thin plates of ε martensite. On the other hand, the morphology of the microstructures of the 20% Mn alloys did not change as the alloy content was increased, Fig. 18a through 18d. Second, the grain size of the 20% Mn alloys containing Mo did not increase as much as the grain size of the 16% Mn alloys containing Mo.

One curious effect was noted in the x-ray phase analysis on the 20% Mn alloys. While no ε martensite was detected in optical microscopy, the x-ray diffraction analysis showed a definite $(110)_\alpha$ peak, and when the integrated intensity of this peak was used to calculate the phase composition, spurious variations in the amount of α martensite was obtained for systematic variations of alloy content. Therefore, the assumption was made that no α martensite existed in the 20% Mn alloys.

F. The Tensile Properties of the 20% Mn Alloys

The tensile properties of the 20% Mn alloys are listed in Table III and shown in Figs. 8, 10, 12 and 19. Note that the yield strength was raised with increasing carbon content, but when 0.5% Mo was added a further increase in the yield strength occurred unlike the case of the 16% Mn alloys. The yield strength of the 20-08-10 alloy decreased because of an increase in its grain size over that of the 20-08-05 alloy. It should be pointed out that the mechanisms which controlled the yield strengths of the 16% Mn alloys still apply to the 20% Mn alloys. The mechanisms just mentioned pertain to the lowering of the M_s and M_d temperatures with increasing alloy content.

The tensile strengths of the alloys varied systematically with changes in the phase content, specifically the ε martensite content. The highest tensile strength of the 20% Mn alloys was produced by the 20-15 alloy which had the most ε martensite in its microstructure before testing. The tensile strength of the 20-00 alloy was limited by austenite instability which produced premature necking. The 20-08-05

and 20-08-10 alloys failed at lower tensile strengths than the 20-15 alloy because the stability of these alloys did not allow as much transformation as in the 20-15 alloy. Therefore the 20-08-05 and 20-08-10 alloys had more martensite at fracture than did the 20-15 alloy. The percent elongations and percent reductions of area did not vary systematically with alloy or phase content.

The stress-strain curve of the 20-15 alloy in Fig. 9 can be compared with the curves of two of the 16% Mn alloys. It is seen that the curve corresponds to a stable austenitic steel whereas the 16% Mn alloys had a much more definite yield point.

G. The Effect of Composition on the Ductile-Brittle Transition Temperature of the 20% Mn Alloys

Figure 20 shows the ductile-brittle transition temperature curves of the 20% Mn alloys. The 20-00 alloy which was mechanically unstable as evidenced by the large amount of necking in a room temperature tensile test, exhibited a transition temperature that was below liquid nitrogen temperature. The addition of carbon to the 20-00 alloy (ie. the 20-15 alloy) produced the same drastic increase in the transition temperature as was produced by the 16-13 alloy (see Fig. 14), and decreased the upper shelf energy by 30 foot-pounds. The scanning electron fractographs in Figs. 22a and c compare the room temperature fracture surfaces of the 20-00 and 20-15 alloys respectively. The pictures indicate that the energy decrease produced in the 20-15 alloy was partially due to cleavage at grain boundaries and partially due to smaller dimples in the rupture surface. The conclusion of this discussion is that while the increased stability of the 20-15 alloy

was beneficial for the tensile properties, the transition temperature properties suffer.

The addition of molybdenum to the 20% Mn alloys caused the transition temperatures of the 20-08-05 and 20-08-10 alloys to be lower than the transition temperature of the 20-15 alloy. The addition of 0.5% Mo caused the transition temperature to be lowered 20°C with respect to the value obtained for the 20-15 alloy while 1.0% Mo caused the transition temperature to be lowered another 15°C. The upper shelf energies of the Mo containing alloys also showed improvement over the value obtained by the 20-15 alloy. The 20-08-05 alloy had the same upper shelf energy as the 20-00 alloy while the 20-08-10 alloy increased the upper shelf energy another 10 foot-pounds. The scanning electron fractograph of the room temperature fracture surface of the 20-08-10 alloy (Fig. 22b) shows larger dimples in the surface than the 20-00 alloy (Fig. 21a). Again, it is noted that ε martensite exhibites a significant role in the liquid nitrogen fracture surface of the 20-08-10 alloy in Fig. 22a, where rectangular outlines indicate cleavage of prior austenite grain boundaries at ε martensite plates.

H. The Effects of Thermal Cycling on the Tensile Properties of the 20% Mn Alloys

Thermal cycling in the 20% Mn alloys produced about the same results as those exhibited by the 16% Mn alloys. The properties of the thermally cycled alloys are listed in Table IV and shown in Figs. 8, 10, 12 and 19. The increase in the yield strengths of the alloys was due to increases in the ε martensite content and the presumed decrease of the M_d temperature (see section D). The ultimate strengths, percent

elongations and percent reductions of area did not vary appreciably over the values obtained in the as quenched condition. The reason for this behavior was that the chemical composition makes the austenite so stable in these steels that the heat treatments do not affect the performance of the materials, and this was borne out by the constancy of the microstructure.

Alloy No.	Phase Composition					
	As Quenched			Thermal Cycled		
	V_α	V_ε	V_γ	V_α	V_ε	V_γ
20-15	-	56	44	-	57	43
20-08-10	-	48	52	-	56	44

IV. CONCLUSIONS

1. Control of the chemical composition and heat treatment was shown to be an effective tool for improving the strength and ductility of the 16%Mn steels.
2. Carbon increased the strength, ductile-brittle transition temperature and the ε-martensite content of the 16%Mn alloys.
3. The addition of molybdenum lowered the ductile-brittle transition temperature of the "plain carbon" 16% and 20%Mn alloys.
4. Thermal cycling increased the strength, ductility and ε-martensite content of the 16%Mn alloys.
5. Thermal cycling increased the strength of the 20%Mn alloys, but had no effect on the ductility.

ACKNOWLEDGEMENTS

The author wishes to communicate his appreciation to Professor Victor F. Zackay and Professor Earl R. Parker for their encouragement and guidance through the course of this investigation. Thanks also go to Professors J. W. Morris, Jr. and F. E. Hauser for their review of the manuscript and to Professor Emeritus S. F. Ravitz for translations of several articles.

The fellowship expressed by many of the students in this research community is also appreciated as well as the many after-hours discussions with Larry Thompson, M. S. Bhat, Warren Garrison, Jr. and John Wert. The support of the staff at the Materials and Molecular Research Division is also gratefully recognized.

This report was done with support from the United States Energy Research and Development Administration.

REFERENCES

1. E. R. Parker and V. F. Zackay, Strong and Ductile Steels, Scientific American 219(5), 36-45 (1968).
2. V. F. Zackay, E. R. Parker, J. W. Morris, Jr., and G. Thomas, LBL-2261, Oct. 1973.
3. M. C. Shaw, Designs for Safety: The Mechanical Fuse, Mechanical Engineering 94(4), 22-29 (1972).
4. V. F. Zackay, E. R. Parker, D. Fahr, and R. Busch, The Enhancement of Ductility in High Strength Steels, ASM Trans. Quart. 60(2), 252 (1967).
5. W. W. Gerberich, P. L. Hemmings, M. D. Merz, and V. F. Zackay, Preliminary Toughness Results on TRIP Steels, Trans. ASM 61, 843-47 (1968).
6. W. W. Gerberich, P. L. Hemmings, and V. F. Zackay, Observations of Strain-Induced Martensite Around a Crack, Trans AIME 245 1124-1126 (1969).
7. J. A. Hall, V. F. Zackay and E. R. Parker, Structure Observations in a Metastable Austenitic Steel, Trans ASM 62, 965-976 (1969).
8. G. R. Chanani, V. F. Zackay, and E. R. Parker, Tensile Properties of 0.05 to 0.20 Pct C TRIP Steels, Met. Trans. 2, 133-139 (1971).
9. D. Fahr, Stress and Strain-Induced Formation of Martensite and Its Effects on Strength and Ductility of Metastable Austenitic Stainless Steels, Met Trans. 2, 1883-1892 (1971).

10. S. D. Antolovich and B. Singh, On the Toughness Increment Associated with the Austenite to Martensite Phase Transformation in TRIP Steels, Met. Trans. 2, 2135-2141 (1971).

11. W. W. Gerberich, P. L. Hemmings, and V. F. Zackay, Fracture and Fractography of Metastable Austenites, Met. Trans. 2, 2243-2253 (1971).

12. D. Bhandarkar, V. F. Zackay, and E. R. Parker, Stability and Mechanical Properties of Some Metastable Austenitic Steels, Met. Trans. 3, 2619-2631 (1972).

13. V. F. Zackay, W. W. Gerberich, and S. F. Ravitz, Mechanical Properties and Corrosion Resistance of TRIP Steels, Lawrence Berkeley Laboratory Report, UCRL 20503, February 1971.

14. R. A. McCoy and W. W. Gerberich, Hydrogen Embrittlement Studies of a TRIP Steel, Met. Trans. 4, 539-547 (1973).

15. W. W. Gerberich, G. Thomas, E. R. Parker, and V. F. Zackay, Metastable Austenites: Decomposition and Strength, Proc. Second Int. Conf. on the Strength of Metals and Alloys, Asilomar, Calif., August 1970, p. 894.

16. J. L. Mihelich and J. H. Smith, New Pipeline Steel for Low Temperature Uses, Metal Progress, April 1974, pp. 39-41.

17. J. P. Bressanelli and A. Moskowitz, Trans ASM, 59, 233 (1966).

18. M. J. Schanfein, M. S. Thesis, U.C. Berkeley, LBL-2749.

19. I. Tamura, T. Maki, M. Aato, Y. Tomota, and M. Okada, Strength and Ductility of Austenitic Iron Alloys Accompanying Strain-Induced Martensitic Transformations; Proc. Second Int. Conf. on the Strength of Metals and Alloys, Asilomar, Calif., August 1970, p. 900.

Table II. Rockwell Hardness.

Alloy No.	R_c	Alloy No.	R_c
16-00	12.5	20-00	18.6
16-05	19.3	20-15	27.0
16-13	26.7	20-08-05	21.5
16-08-05	16.0	20-08-10	20.5
16-08-10	17.5		

Table III. Tensile Test Data - As Quenched Alloys.

Alloy No.	Yield Strength (ksi)	Ultimate Strength (ksi)	Percent Elongation	Percent Reduction of Area
16-00*	30	101	30	71
16-05	50	122	38	73
16-13	60	175	28	20
16-08-05	47	153	34	35
16-08-10	46	150	46	51
20-00*	61	101	34	70
20-15	68	150	44	41
20-08-05	71	140	43	37
20-08-10	59	126	38	44

*data from M. Schanfein.[18]

20. D. J. Drobnjak and J. Gordon-Parr, Deformation Substructure and Strain Hardening Characteristics of Metastable Fe-Mn Austenites, Met. Trans, 1, 759-765 (1970).

21. D. J. Drobnjak and J. Gordon-Parr, Thermomechanical Treatment and Transformation Characteristics of Fe-Mn Austenites, Met. Trans. 1, 1521-1526 (1970).

22. D. Dulieu and J. Nutting, Iron and Steel Inst. Special Report No. 86, 1964, p. 140.

23. J. Gordon-Parr, X-Ray Investigation of the Epsilon Phase in an Fe-Mn Alloy, JISI, June 1952, p. 137.

24. H. Schumann and F. Heider, Effect of Repeated Phase Transitions on the $\gamma \rightleftharpoons \varepsilon$ Transformation in Austenitic Manganese Steels, Z. Metallkunde 56, 165-172 (1965).

25. H. Schumann, Martensitic Transformations in Low Carbon Manganese Steels, Arch. Eisenhuttenwesen 39, 647-656 (1967).

26. A. Holden, J. D. Bolton, E. R. Petty, Structure and Properties of Iron-Manganese Alloys, JISI, Sept. 1971, p. 721.

27. P. L. Mangonon, Jr. and G. Thomas, UCRL-18868 preprint, June 1969.

28. K. Suemune and T. Ooka, Electron Microscopic Structures of Iron-Manganese Alloys; Nippon Kinzuko Gakkai-Si, 30(5), 428-434 (1966).

29. J. Dash and H. M. Otte, Acta Met. 11, 1169 (1963).

30. J. Gordon-Parr, Acta Cryst. 5, 842 (1952).

Table 1. Chemical Composition of Alloys.

Alloy Designation	Weight Percent			
	Mn	C	Mo	Fe
16-00*	16.0	--	--	Balance
16-05	16.3	0.045	--	↓
16-13	16.0	0.13	--	↓
16-08-05	16.1	0.07	0.51	↓
16-08-10	16.3	0.08	0.94	↓
20-00*	19.5	--	--	Balance
20-15	19.8	0.15	--	↓
20-08-05	20.2	0.08	0.46	↓
20-08-10	20.1	0.08	0.97	↓

*data from M. Schanfein.[18]

Table IV. Tensile Test Data - Thermal Cycled Alloys

Alloy No.	Heat Treat cycle	Yield Strength (ksi)	Ultimate Strength (ksi)	Percent Elongation	Percent Reduction of Area
16-00	--	--	--	--	--
16-05	2B	58	124	34	72
16-13	2B	64	179	40	54
16-08-05	2B	53	158	40	53
16-08-10	3B	61	156	53	56
20-00	--	--	--	--	--
20-15	1B	81	152	43	43
20-08-05	1B	77	141	40	37
20-08-10	3B	78	149	41	45

Table V. Phase Composition ~ As Quenched Alloys.

Alloy No.	Percent of Phases		
	α	ε	γ
16-00	25	47	28
16-05	10	55	35
16-13	4	67	29
16-08-05	5	66	29
16-08-10	4	63	33
20-00	--	48	52
20-15	--	56	44
20-08-05	--	51	49
20-08-10	--	48	52

Table VI. Phase Composition after Tensile Deformation

	Percent of Phases		
Alloy No.	α	ε	γ
16-00*	92	-	8
16-05	83	17	-
16-13	74	26	-
16-08-05	76	21	3
16-08-10	64	33	3
20-00*	18	51	31
20-15	15	75	10
20-08-05	8	80	12
20-08-10	3	74	23

*Data from M. Schanfein[18]

FIGURE CAPTIONS

Fig. 1. Schematic representation of the mechanical properties versus test temperature for annealed TRIP steels based on reference 19.

Fig. 2. Phase transformation temperatures for slowly cooled Fe-Mn alloys from reference 18.

Fig. 3. A material processing diagram showing the experimental techniques used in the investigation.

Fig. 4. A schematic diagram of the thermal cycling heat treatment.

Fig. 5. Standard ASTM E23-72 and E8-69 Charpy V-notch and tensile specimens respectively.

Fig. 6. Optical micrographs of austenitized and quenched 16% Mn alloys; (a) 16% Mn, (b) 16% Mn-0.05% C, (c) 16% Mn-0.13% C, (d) 16% Mn-0.08% C-0.5% Mo.

Fig. 7. Enlarged optical micrograph of 16% Mn alloy showing α-martensite in ε-martensite at A and α-martensite in γ at B.

Fig. 8. Strengths vs carbon content for the austenitized and quenched, and thermal cycled 16% and 20% Mn alloys.

Fig. 9. Schematic of stress-strain curves showing the discontinuous plastic flow characteristic of strain induced transformations.

Fig. 10. Percent elongation and percent reduction of area vs carbon content for the 16% and 20% Mn alloys.

Fig. 11. Scanning electron fractographs of the 16% Mn-0.13% C tensile specimen showing fracture along ε-martensite plates in (b).

Fig. 12. Strengths vs molybdenum content for the 16% and 20% Mn alloy containing 0.08% C.

Fig. 13. Percent elongation and percent reduction of area vs molybdenum content for the 16% Mn alloys.

Fig. 14. Charpy V-notch impact toughness vs test temperature for the austenitized and quenched 16% Mn alloys (see Table I).

Fig. 15. Scanning electron fractographs of the austenitized and quenched 16% Mn alloy (a) tested at 23°C, (b) tested at -196°C and the 16% Mn-0.13% C alloy (c) tested at 23°C (d) tested at -196°C.

Fig. 16. Scanning electron x-ray analysis of particles in Fig. 15(b).

Fig. 17. Scanning electron fractographs of the austenitized and quenched 16% Mn-0.08% C-1.0% Mo alloy (a) tested at -196°C, (b) tested at 23°C.

Fig. 18. Optical micrographs of austenitized and quenched 20% Mn alloys; (a) 20% Mn, (b) 20% Mn-0.15% C, (c) 20% Mn-0.08% C-0.5% Mo, (d) 20% Mn-0.08% C-1.0% Mo.

Fig. 19. Percent elongation and percent reduction of area vs. molybdenum content for the 20% Mn alloys.

Fig. 20. Charpy V-notch impact toughness vs test temperature for austenitized and quenched 20% Mn alloys (see Table I).

Fig. 21. Scanning electron fractographs of the austenitized and quenched 20% Mn alloy (a) tested at 23°C, (b) tested at -196°C and the 20% Mn-0.15% C alloy (c) tested at 23°C, (d) tested at -196°C.

Fig. 22. Scanning electron fractographs of the austenitized and quenched 20% Mn-0.08% C-1.0% Mo alloy (a) tested at -196°C and (b) tested at 23°C.

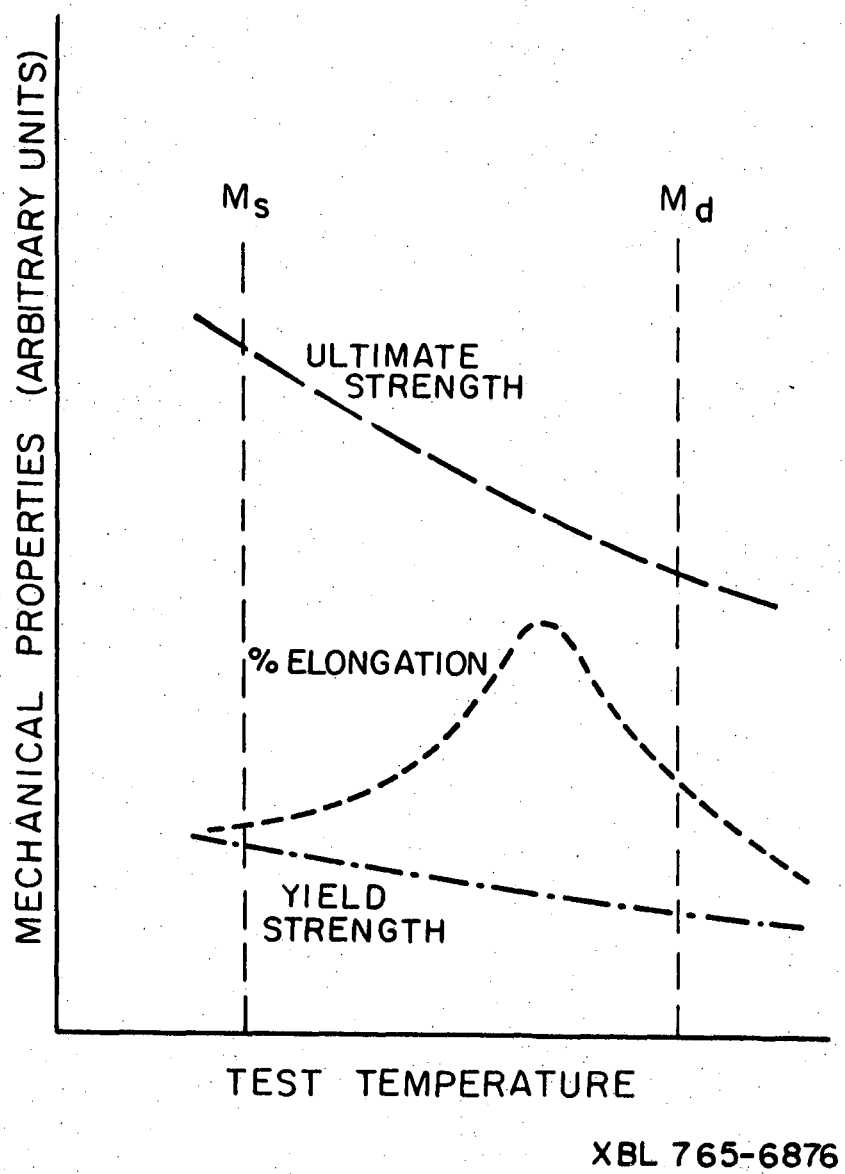

Fig. 1.

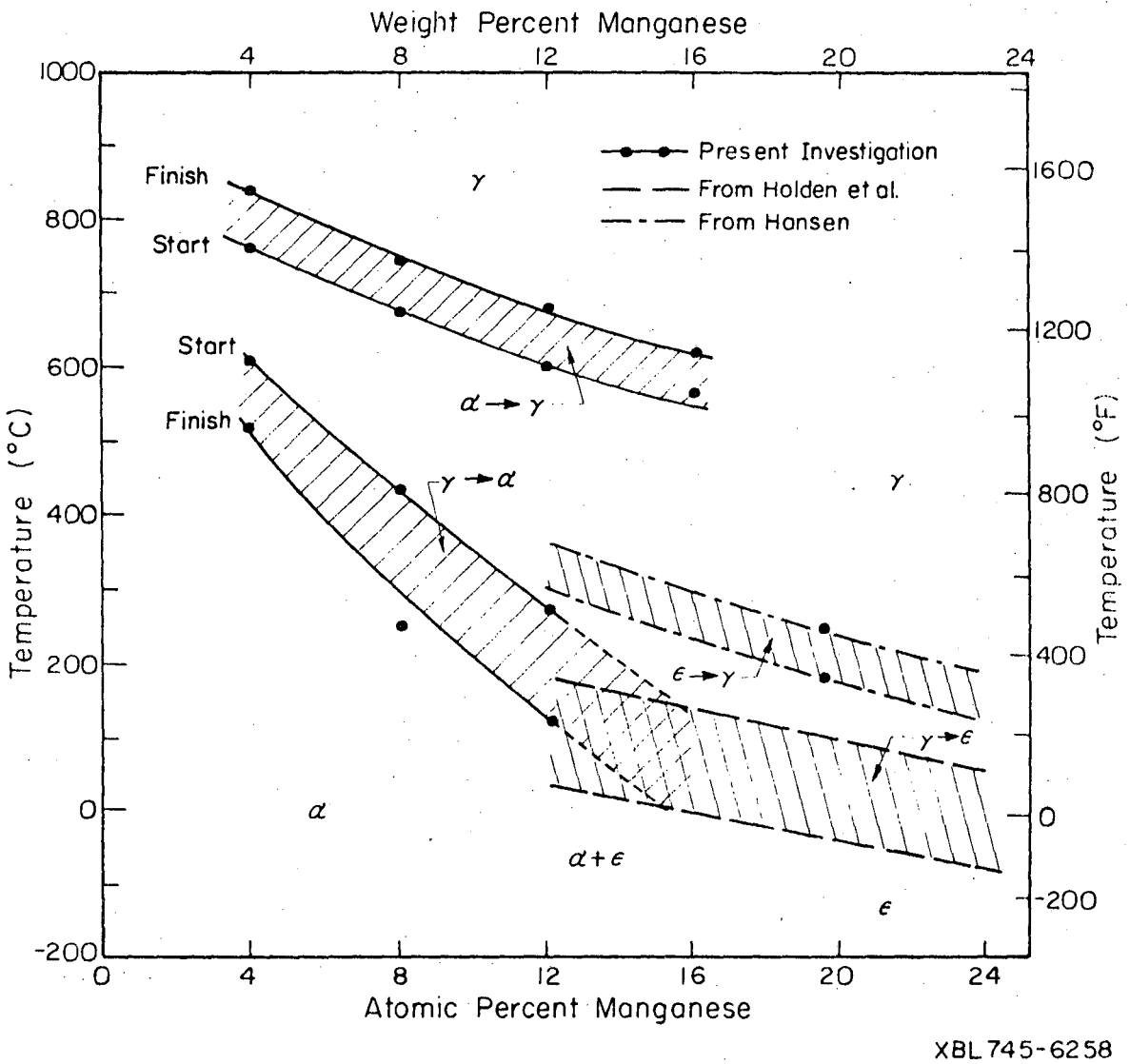
Weight Percent Manganese
4
8
12
16
20
24
1000
800
600
400
200
0
-200
Temperature (°C)
1600
1200
800
400
0
-200
Temperature (°F)
Present Investigation
From Holden et al.
From Hansen
Finish
Start
Start
Finish
γ
α → γ
γ → α
γ
ε → γ
γ → ε
α
α+ε
ε
0
4
8
12
16
20
24
Atomic Percent Manganese
XBL745-6258

Fig. 2.

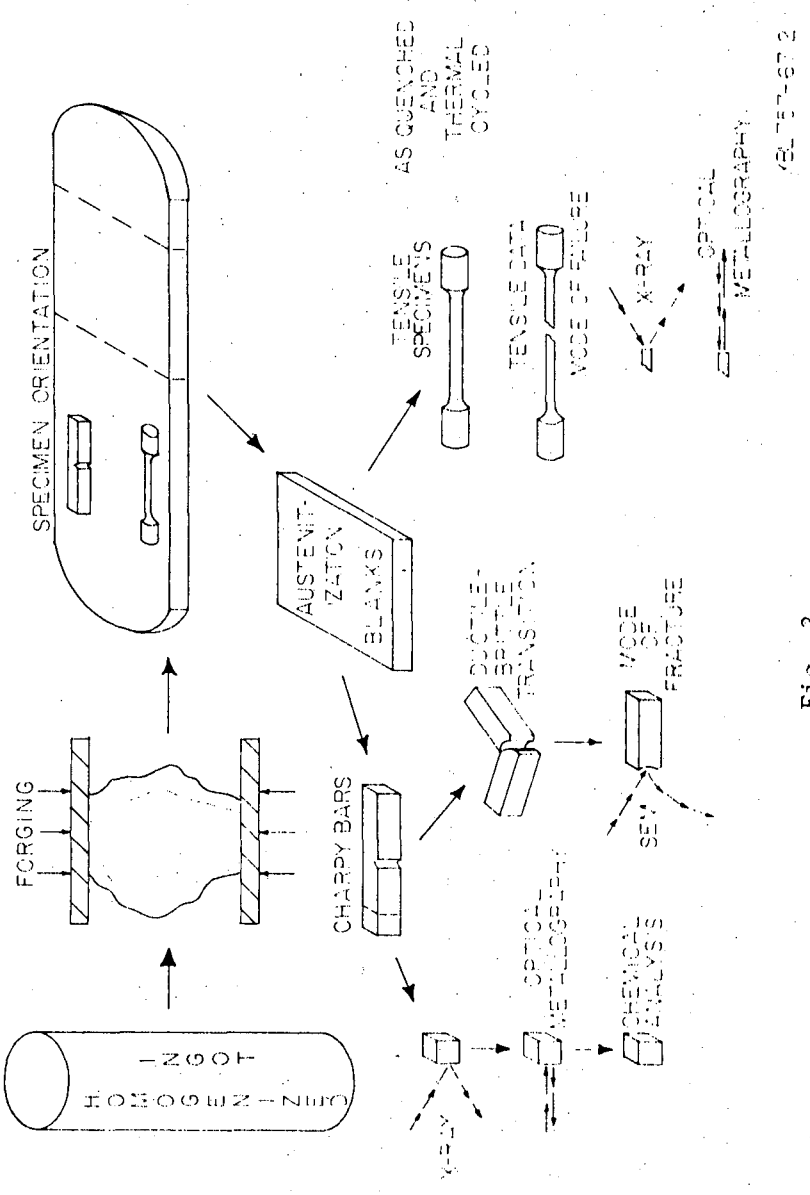

Fig. 3.

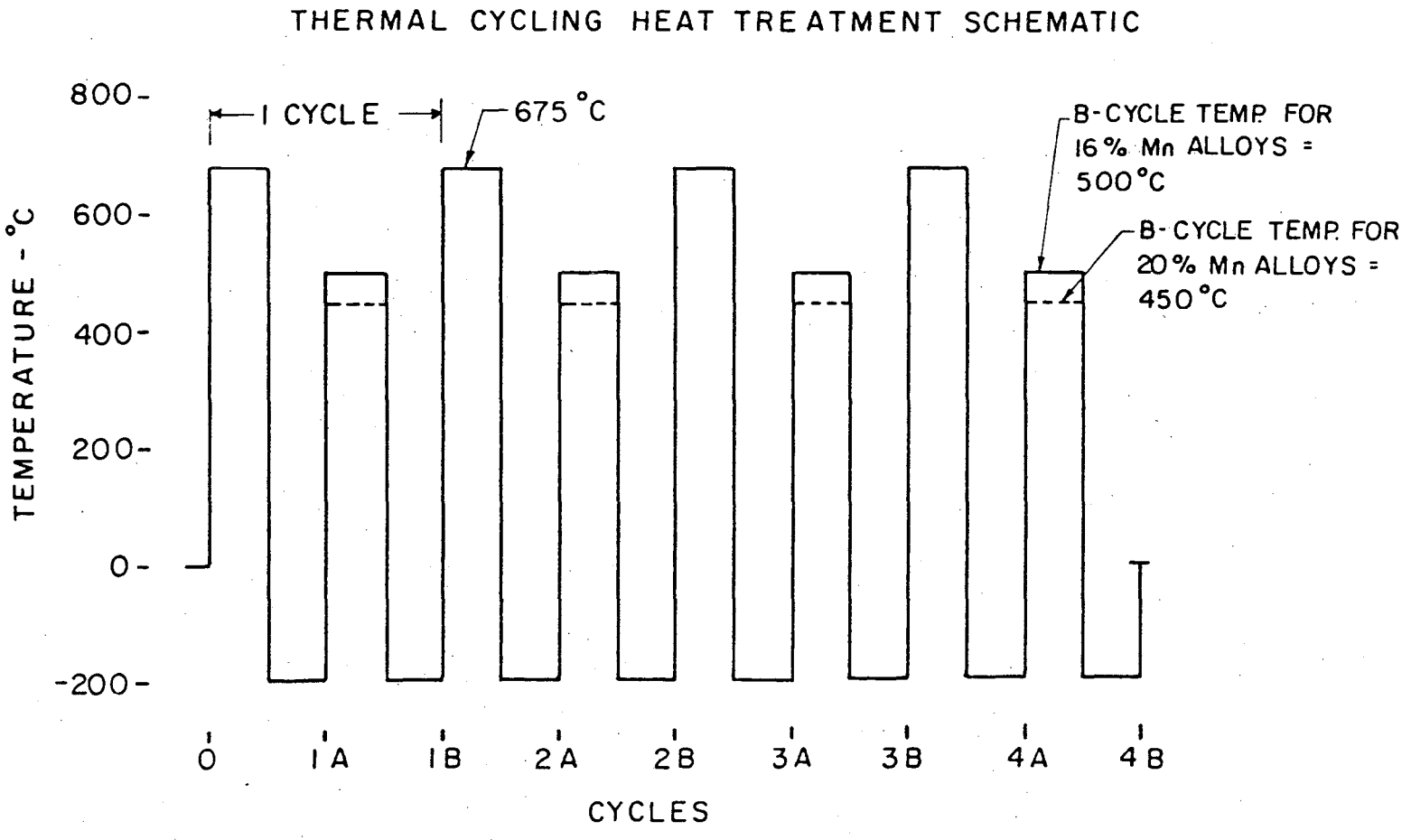
THERMAL CYCLING HEAT TREATMENT SCHEMATIC
800-
600-
400-
200-
0-
-200-
TEMPERATURE - °C
1 CYCLE
675 °C
B-CYCLE TEMP. FOR
16% Mn ALLOYS =
500°C
B-CYCLE TEMP. FOR
20% Mn ALLOYS =
450°C
0
1A
1B
2A
2B
3A
3B
4A
4B
CYCLES
XBL765-6873

Fig. 4.

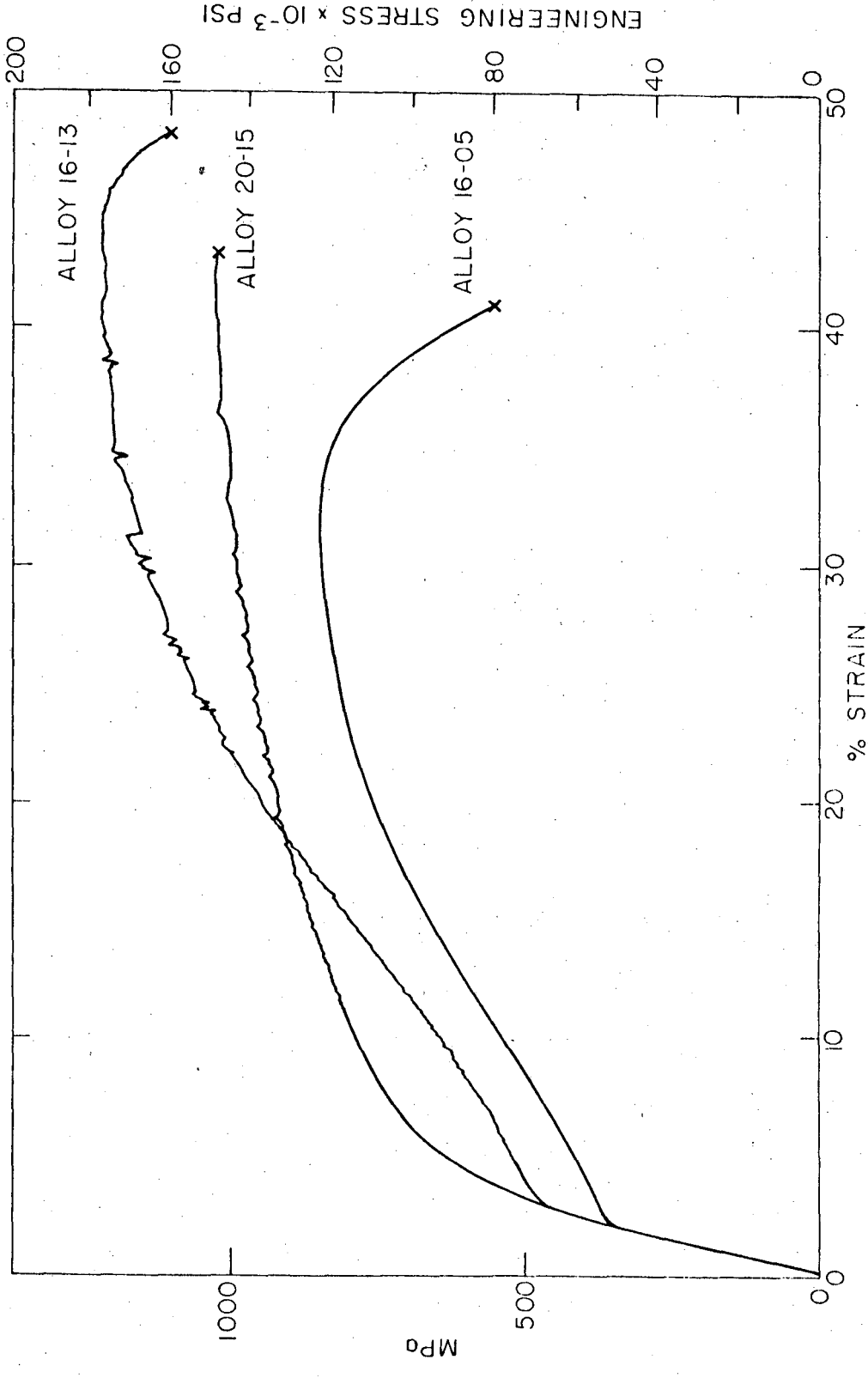

Fig. 9.

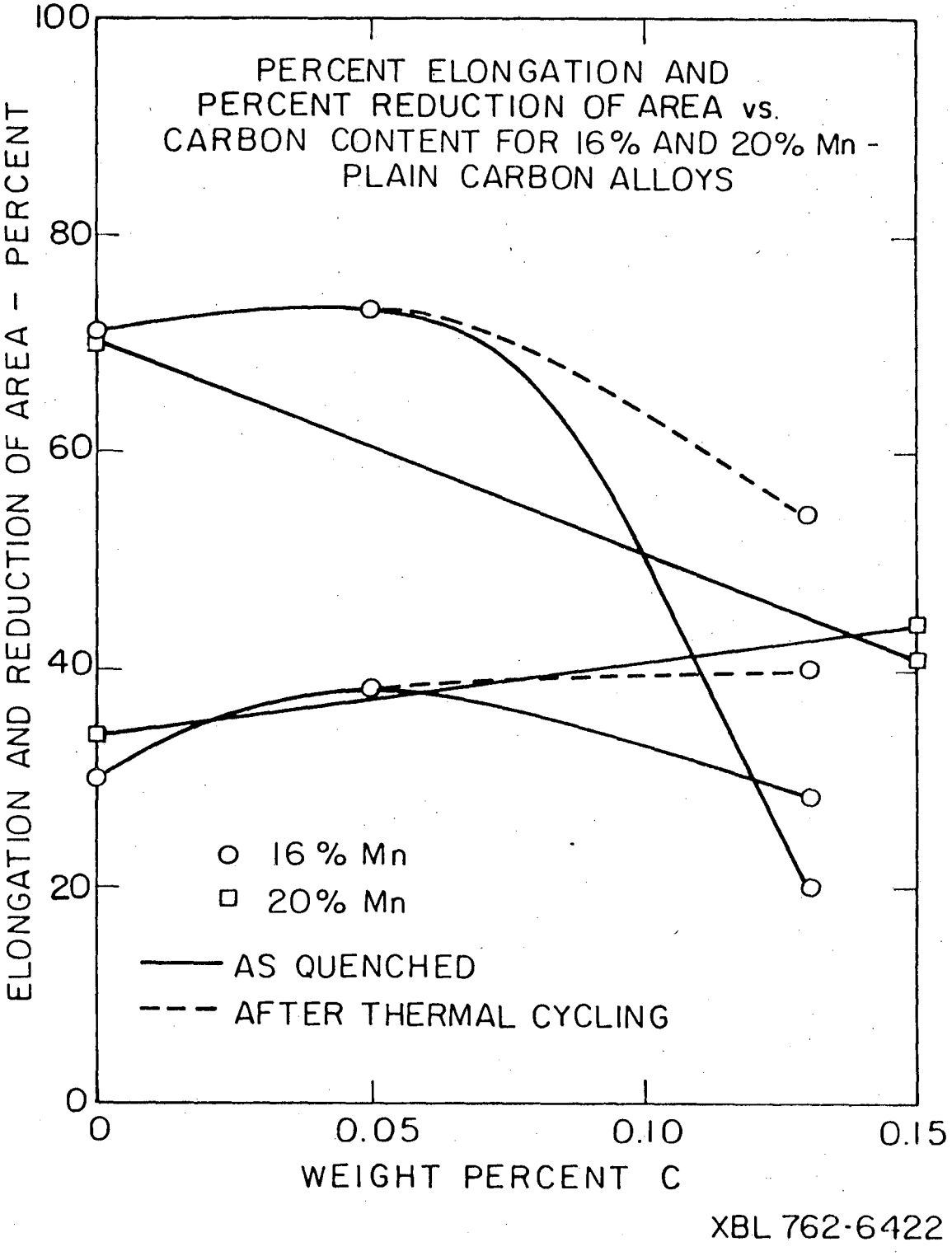
PERCENT ELONGATION AND
PERCENT REDUCTION OF AREA vs.
CARBON CONTENT FOR 16% AND 20% Mn -
PLAIN CARBON ALLOYS
ELONGATION AND REDUCTION OF AREA - PERCENT
100
80
60
40
20
0
0
0.05
0.10
0.15
WEIGHT PERCENT C
16 % Mn
20% Mn
AS QUENCHED
AFTER THERMAL CYCLING
XBL 762-6422

Fig. 10.

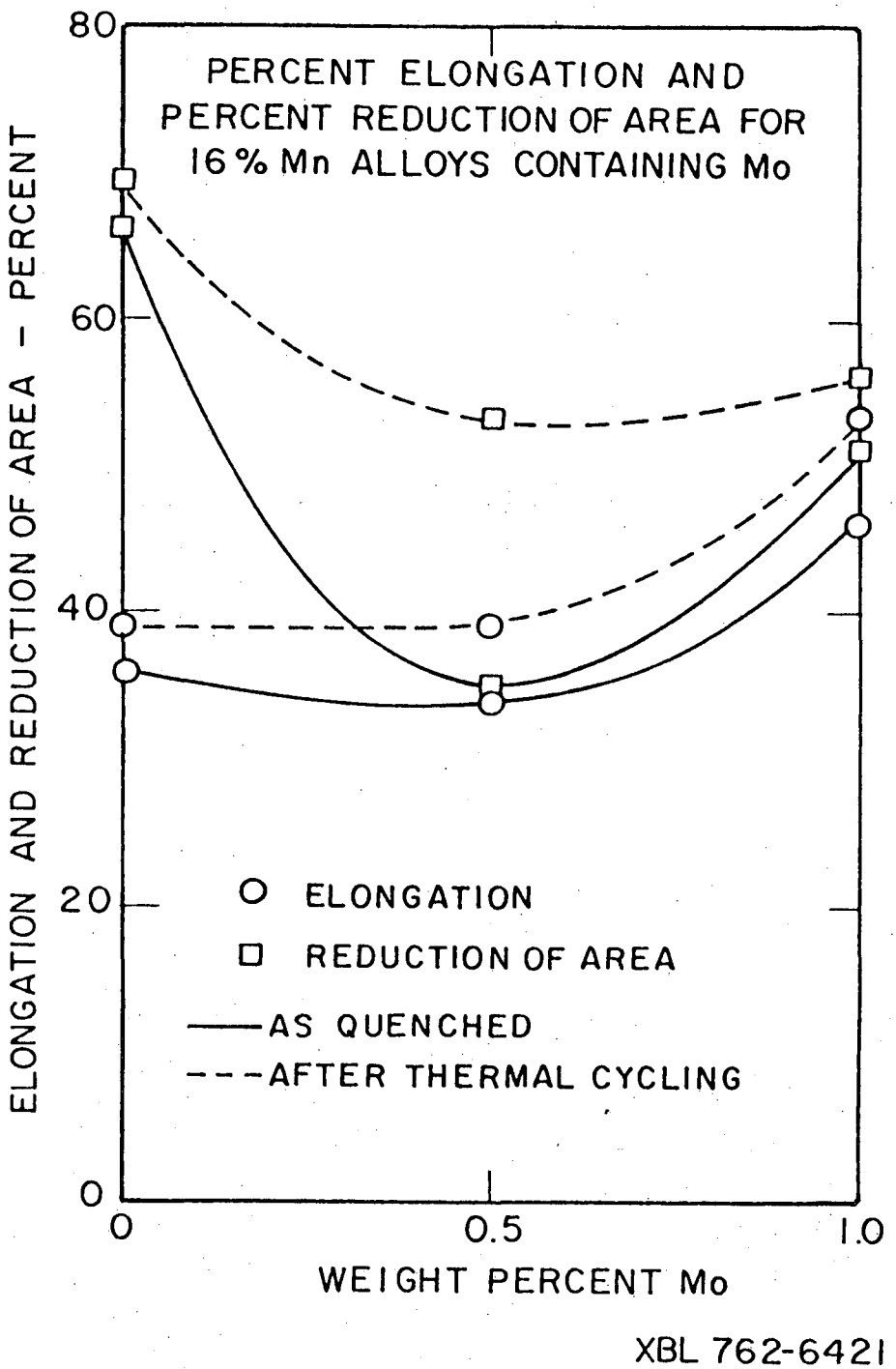

Fig. 13.

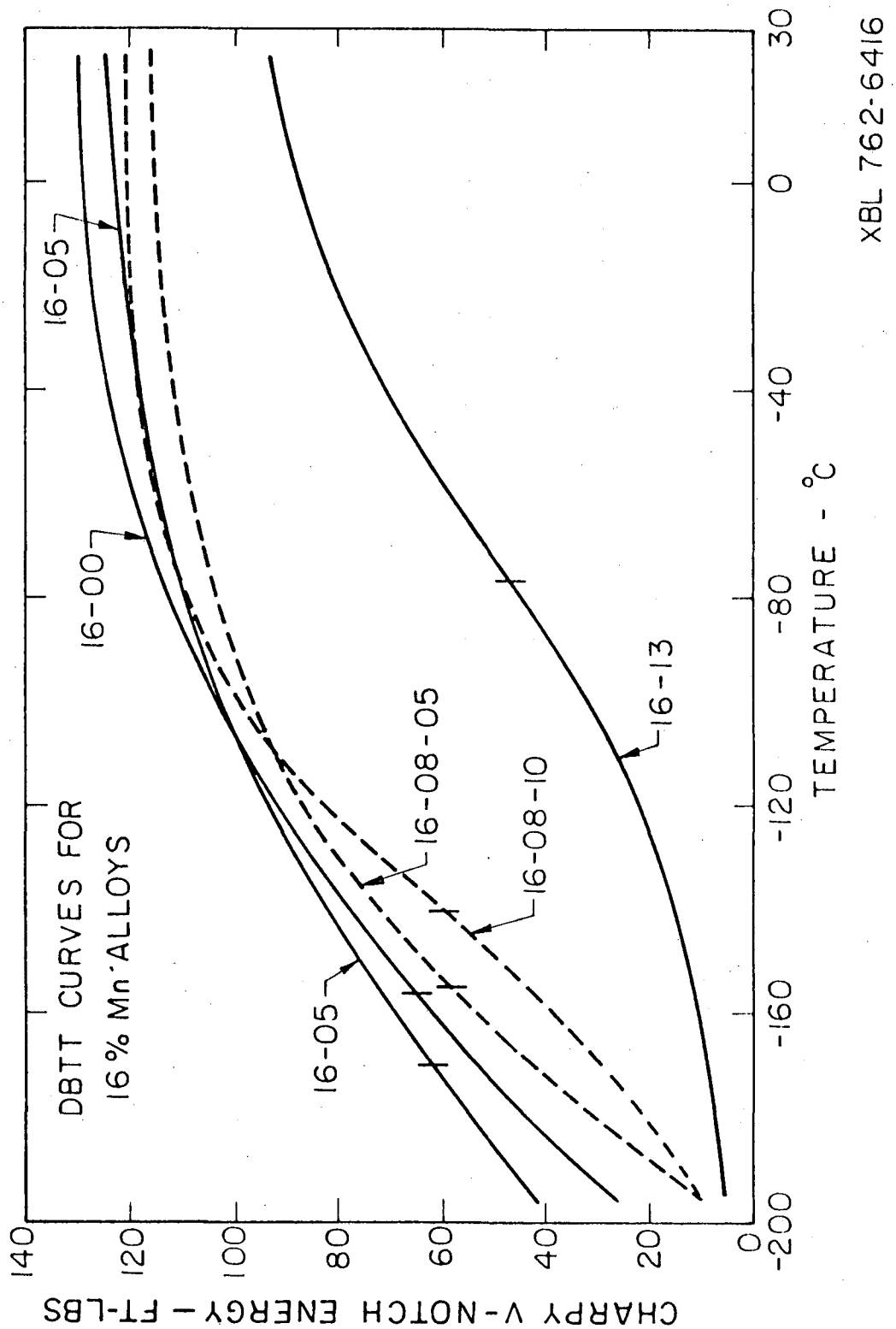
DBTT CURVES FOR
16 % Mn ALLOYS
16-05
16-00
16-05
16-08-05
16-08-10
16-13
CHARPY V-NOTCH ENERGY – FT-LBS
TEMPERATURE - °C
140
120
100
80
60
40
20
0
-200
-160
-120
-80
-40
0
30
XBL 762-6416

Fig. 14.

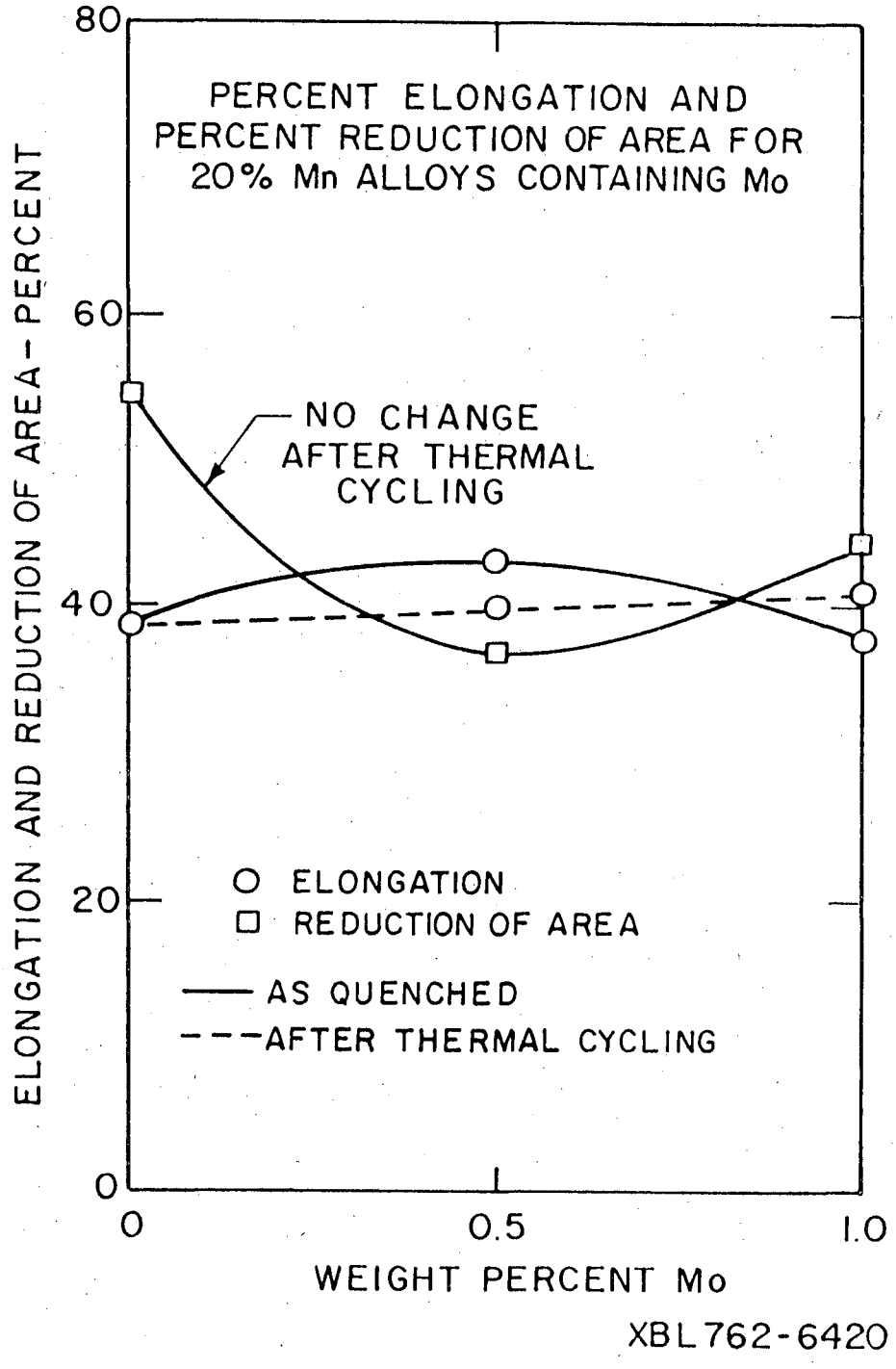

Fig. 19.

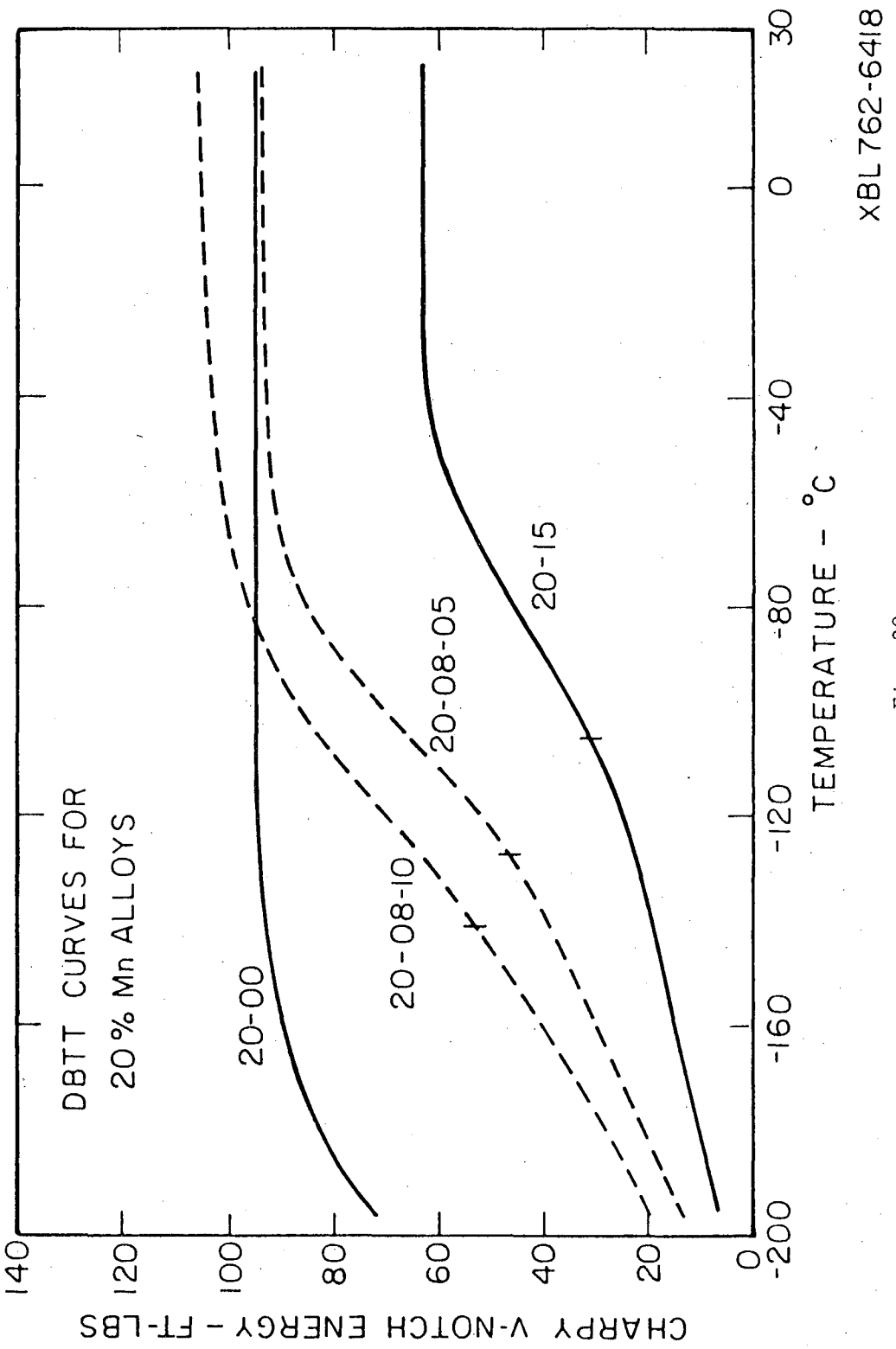
DBTT CURVES FOR
20% Mn ALLOYS
20-00
20-08-10
20-08-05
20-15
CHARPY V-NOTCH ENERGY - FT-LBS
TEMPERATURE - °C
140
120
100
80
60
40
20
0
-200
-160
-120
-80
-40
0
30
XBL 762-6418

Fig. 20.

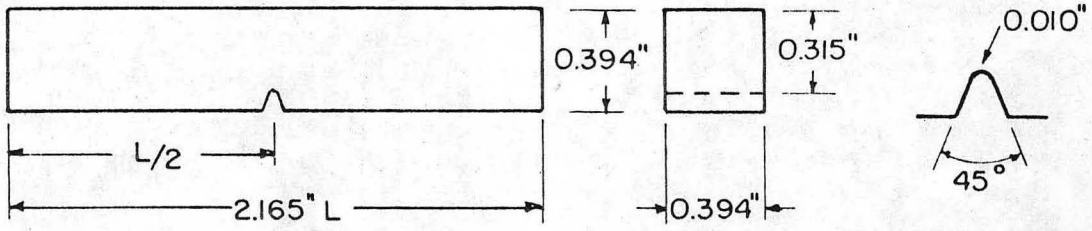

(a) CHARPY V-NOTCH IMPACT SPECIMEN

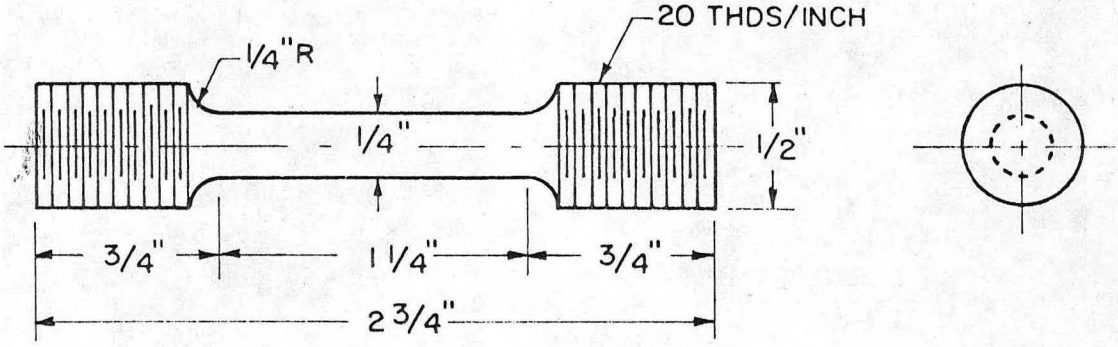

(b) ROUND TENSILE SPECIMEN

XBL735-6189

Fig. 5.

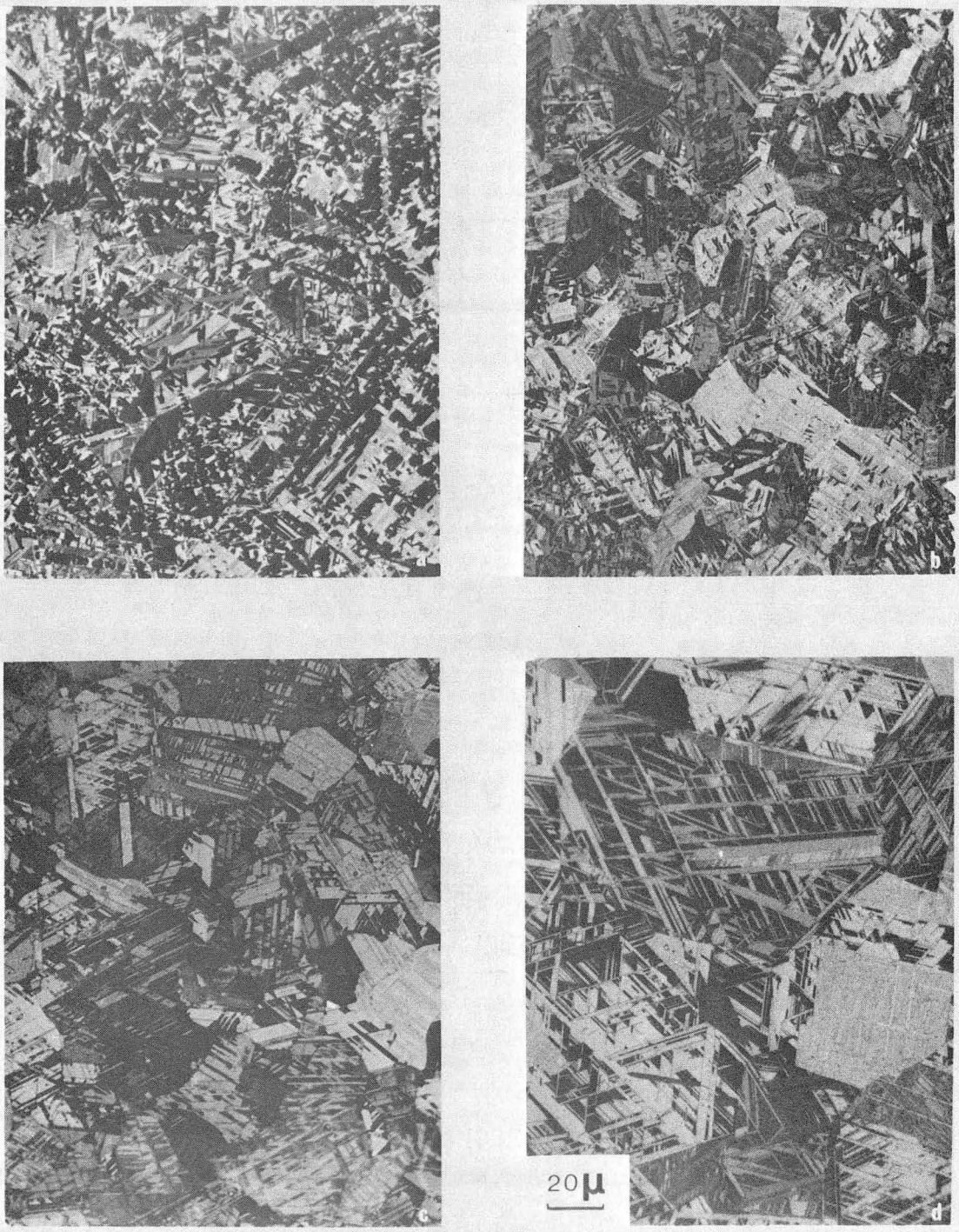

XBB 763-2177

Fig. 6.

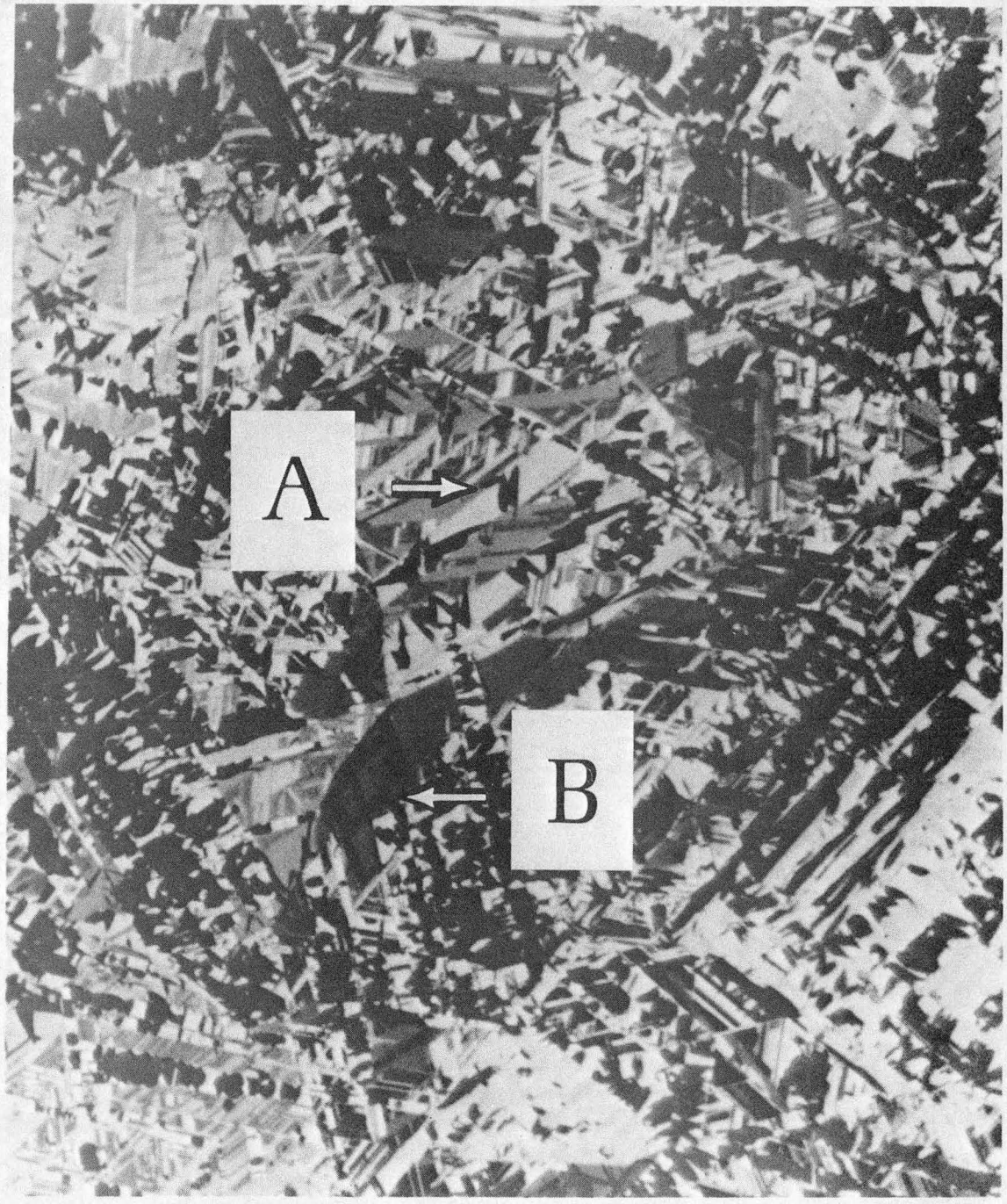

XBB 766-4696

Fig. 7.

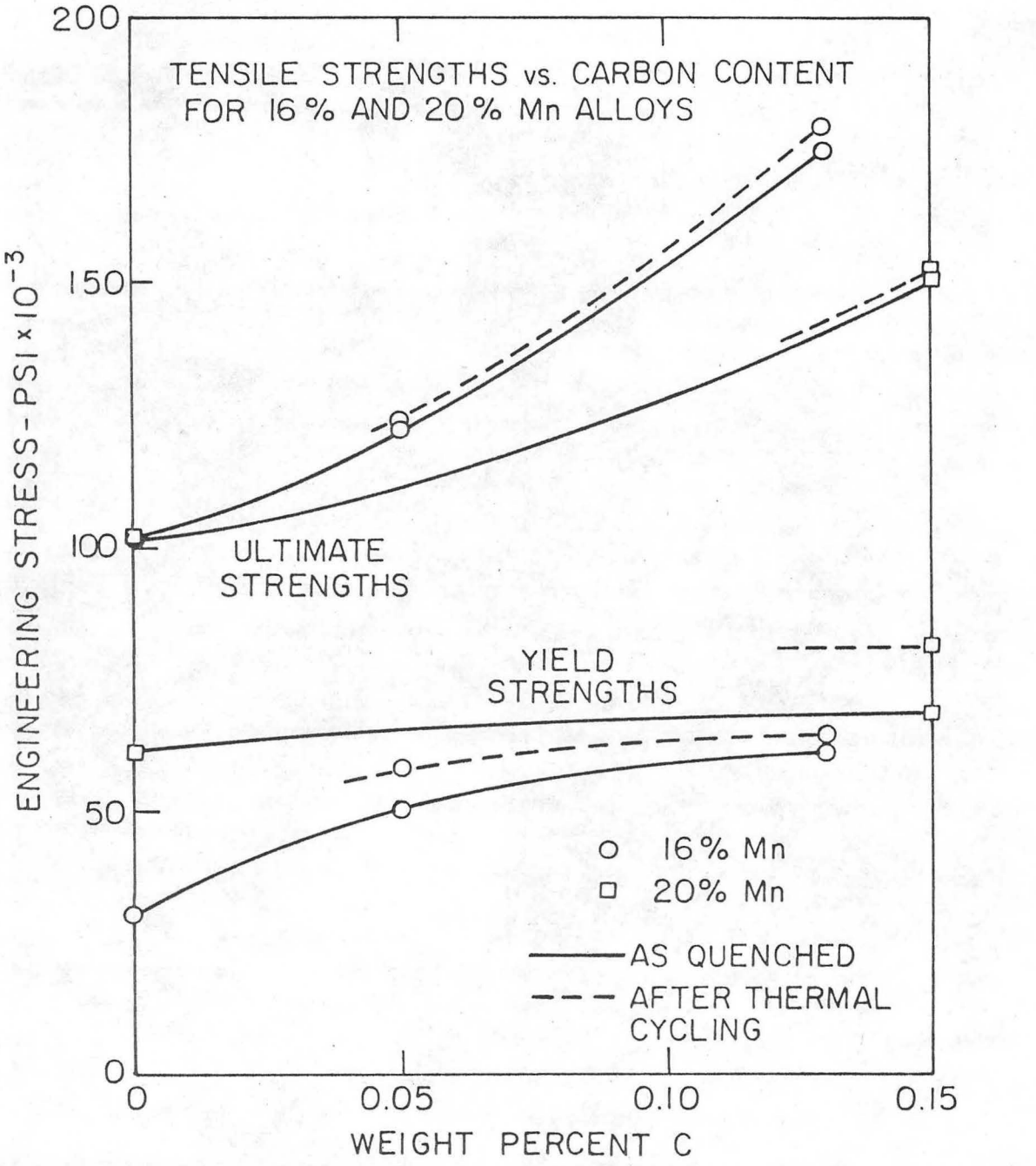
TENSILE STRENGTHS vs. CARBON CONTENT
FOR 16 % AND 20 % Mn ALLOYS
ENGINEERING STRESS - PSI x 10⁻³
200
150
100
50
0
ULTIMATE
STRENGTHS
YIELD
STRENGTHS
16 % Mn
20% Mn
AS QUENCHED
AFTER THERMAL
CYCLING
0
0.05
0.10
0.15
WEIGHT PERCENT C
XBL 762-6423

Fig. 8.

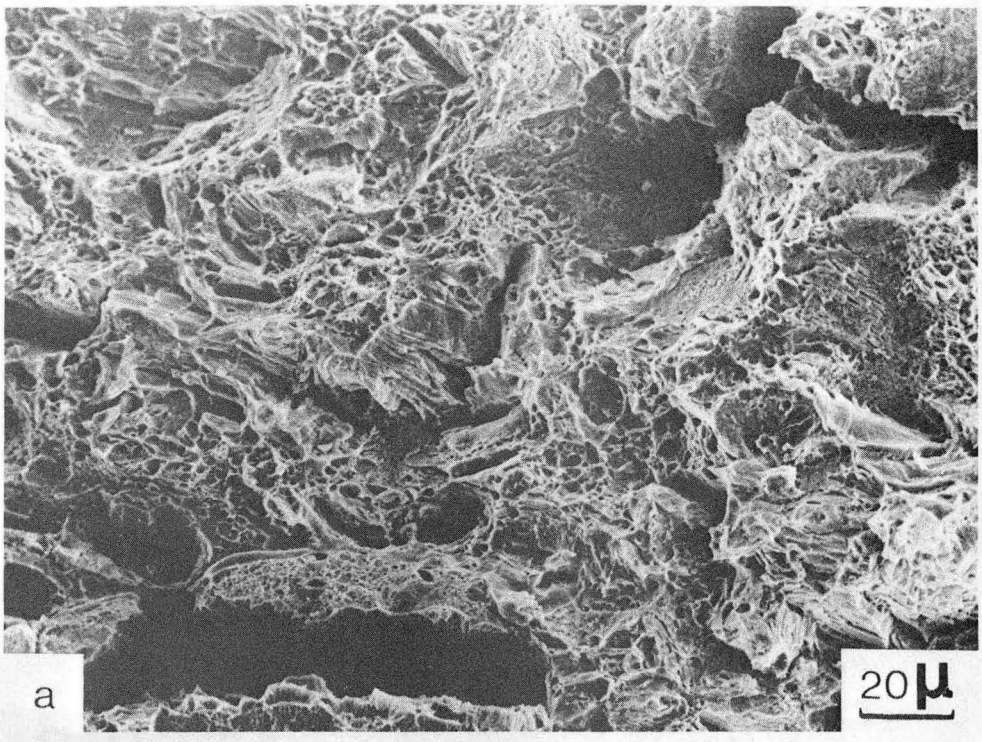

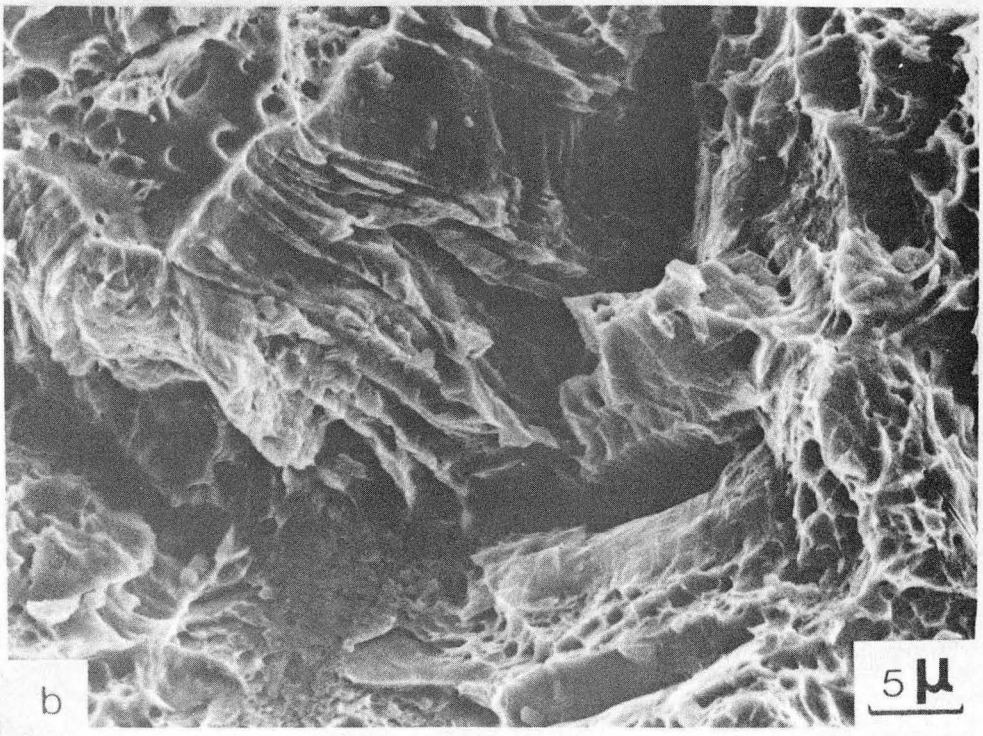

XBB 766-4698

Fig. 11.

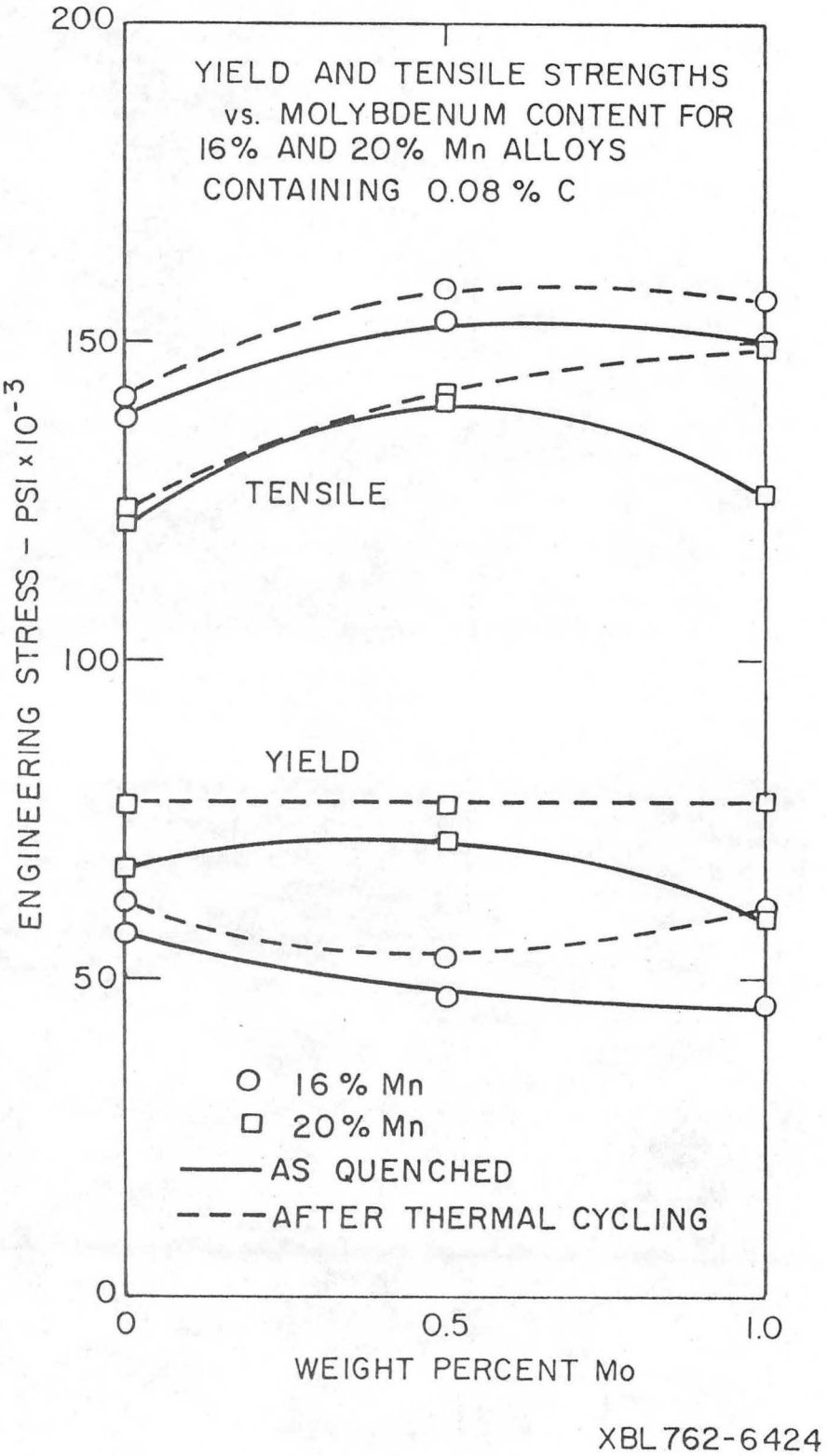
YIELD AND TENSILE STRENGTHS
vs. MOLYBDENUM CONTENT FOR
16% AND 20% Mn ALLOYS
CONTAINING 0.08 % C
ENGINEERING STRESS - PSI x 10⁻³
200
150
100
50
0
TENSILE
YIELD
O 16 % Mn
□ 20 % Mn
AS QUENCHED
AFTER THERMAL CYCLING
0
0.5
1.0
WEIGHT PERCENT Mo
XBL 762-6424

Fig. 12.

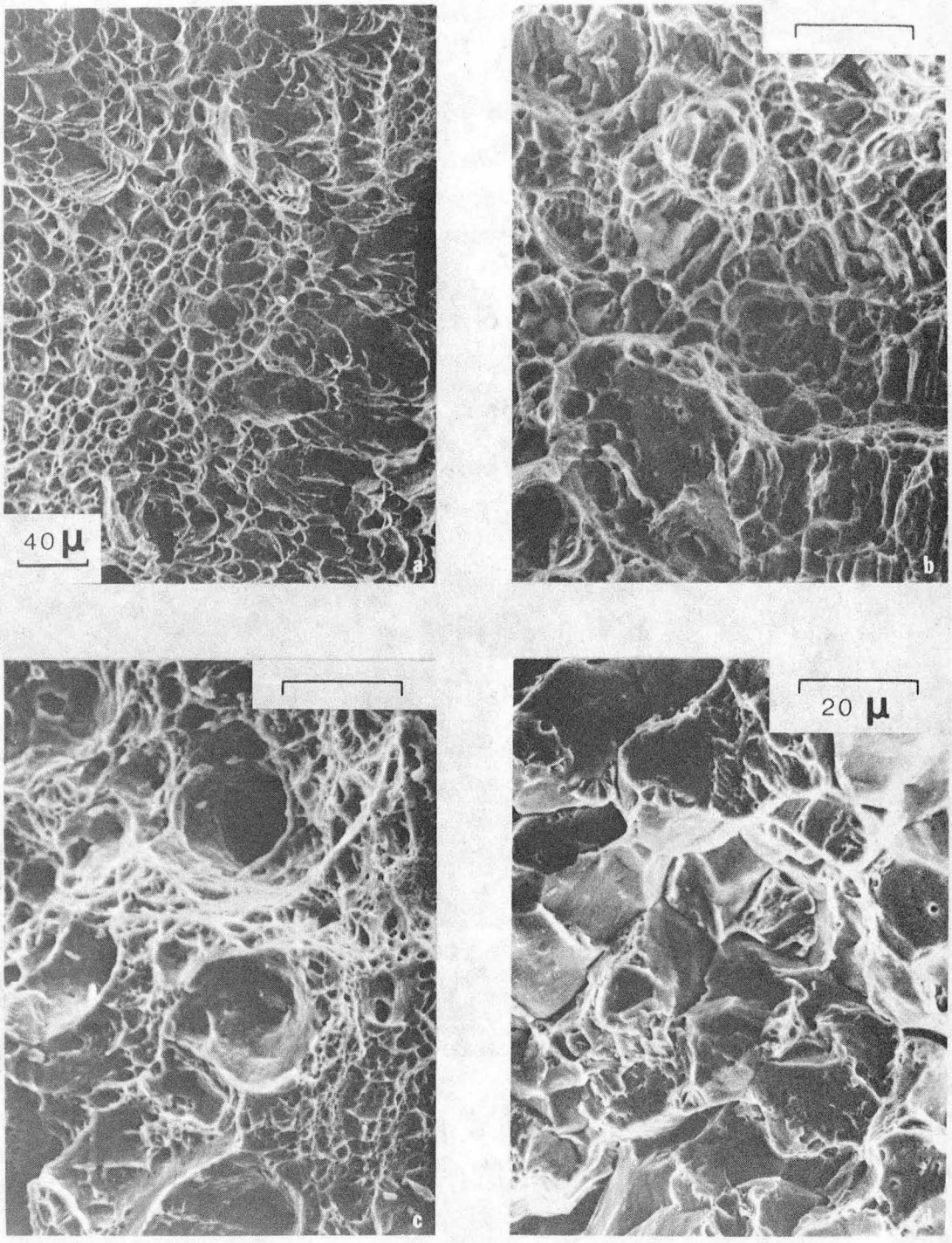

XBB 763-2178

Fig. 15.

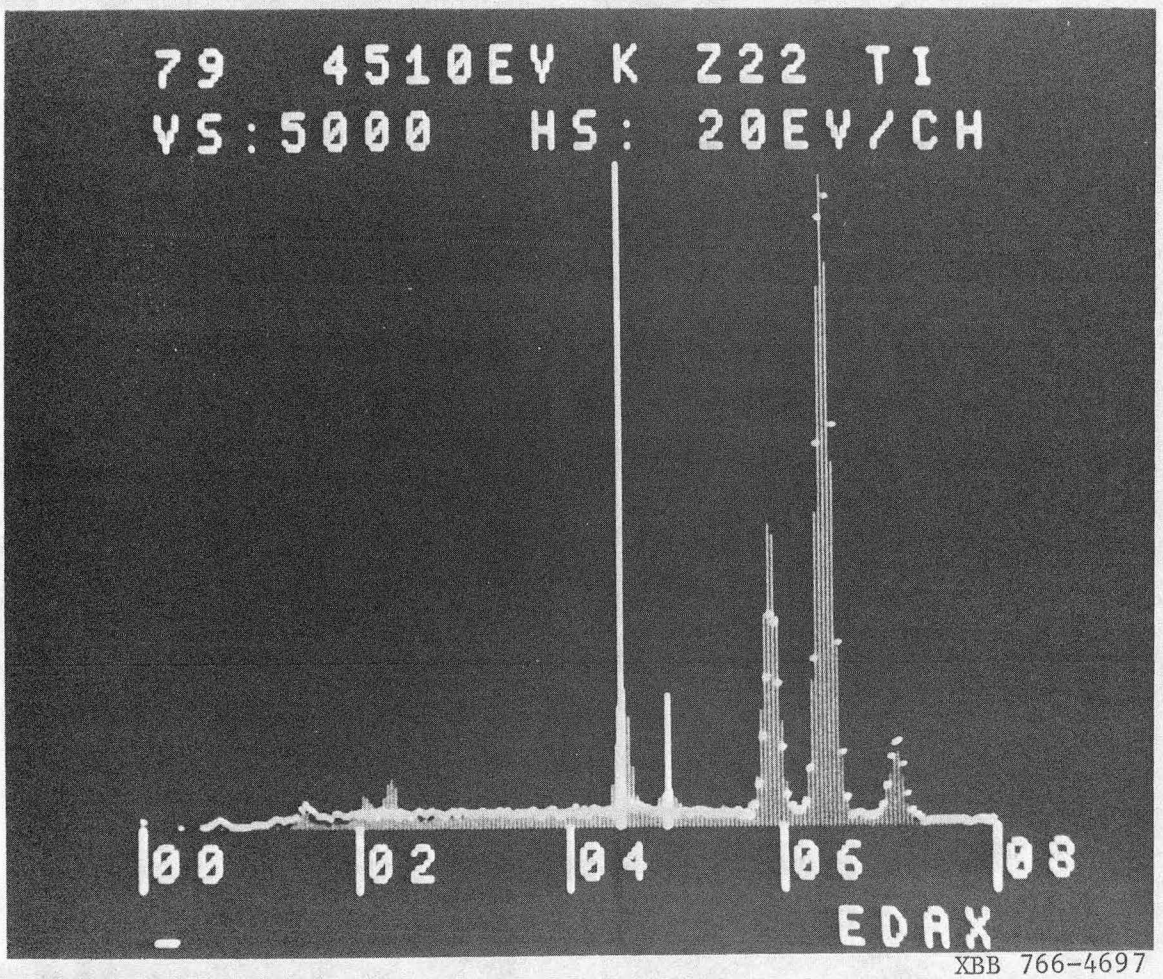

XBB 766-4697

Fig. 16.

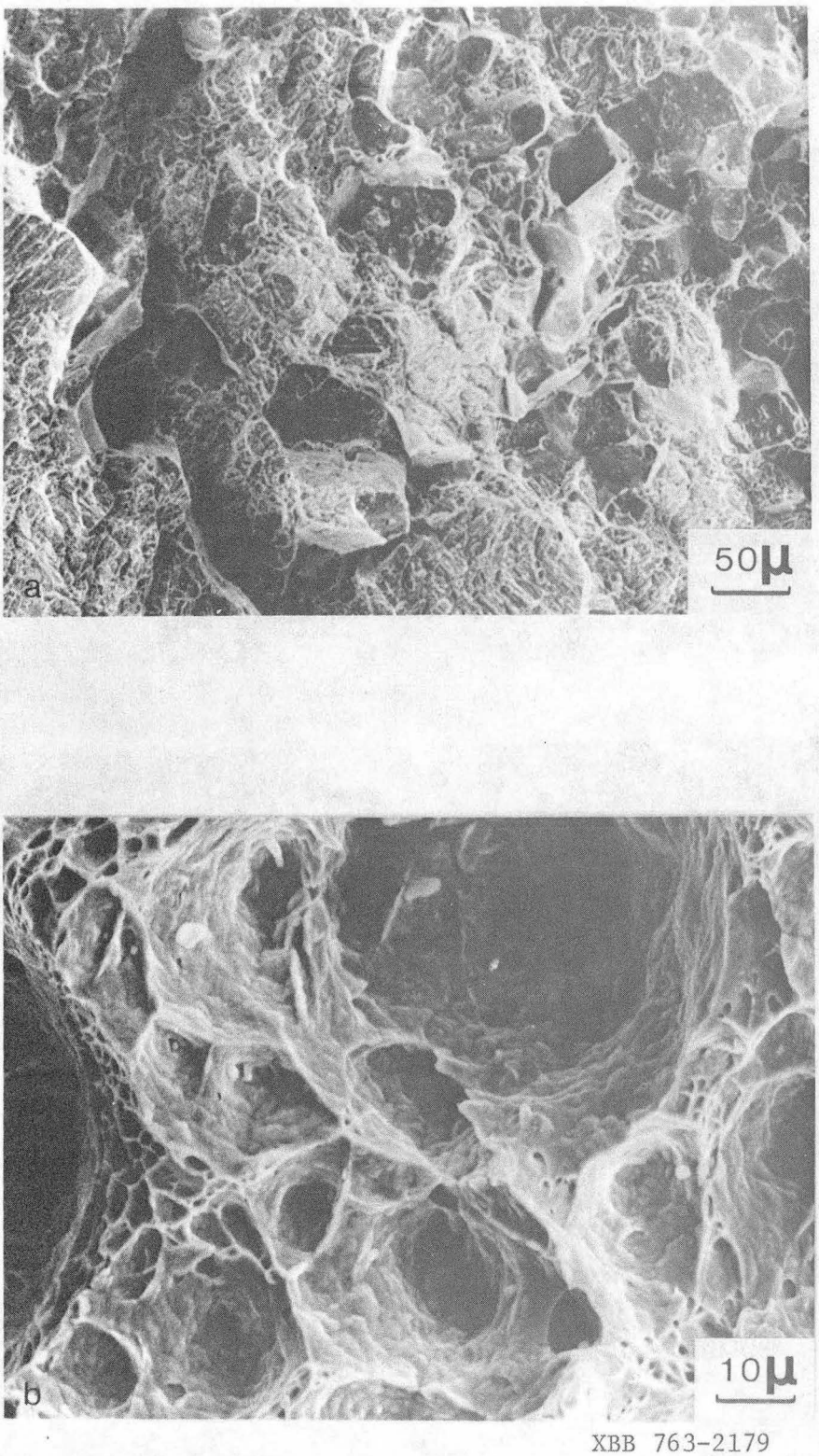

XBB 763-2179

Fig. 17.

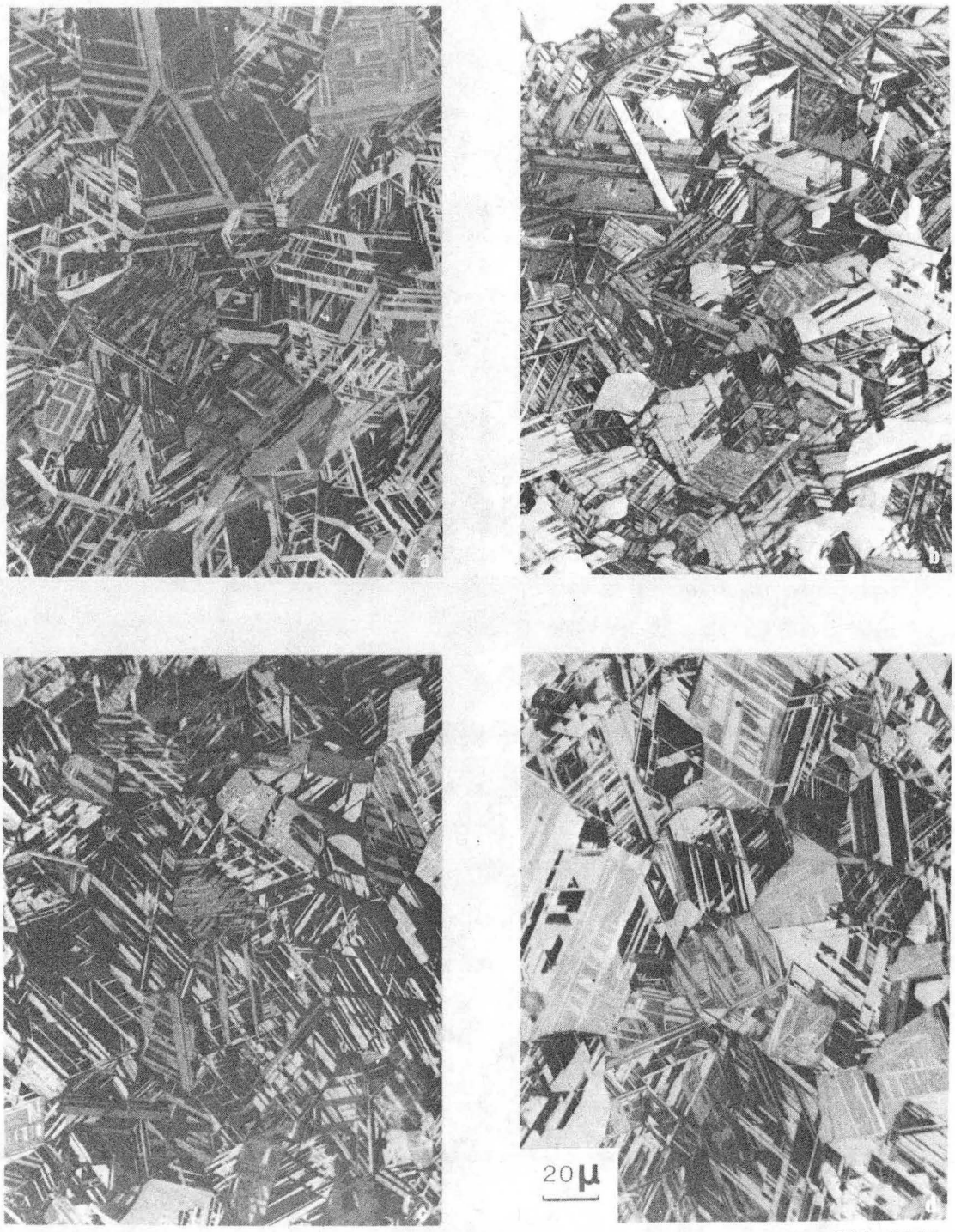

XBB 763-2181

Fig. 18.

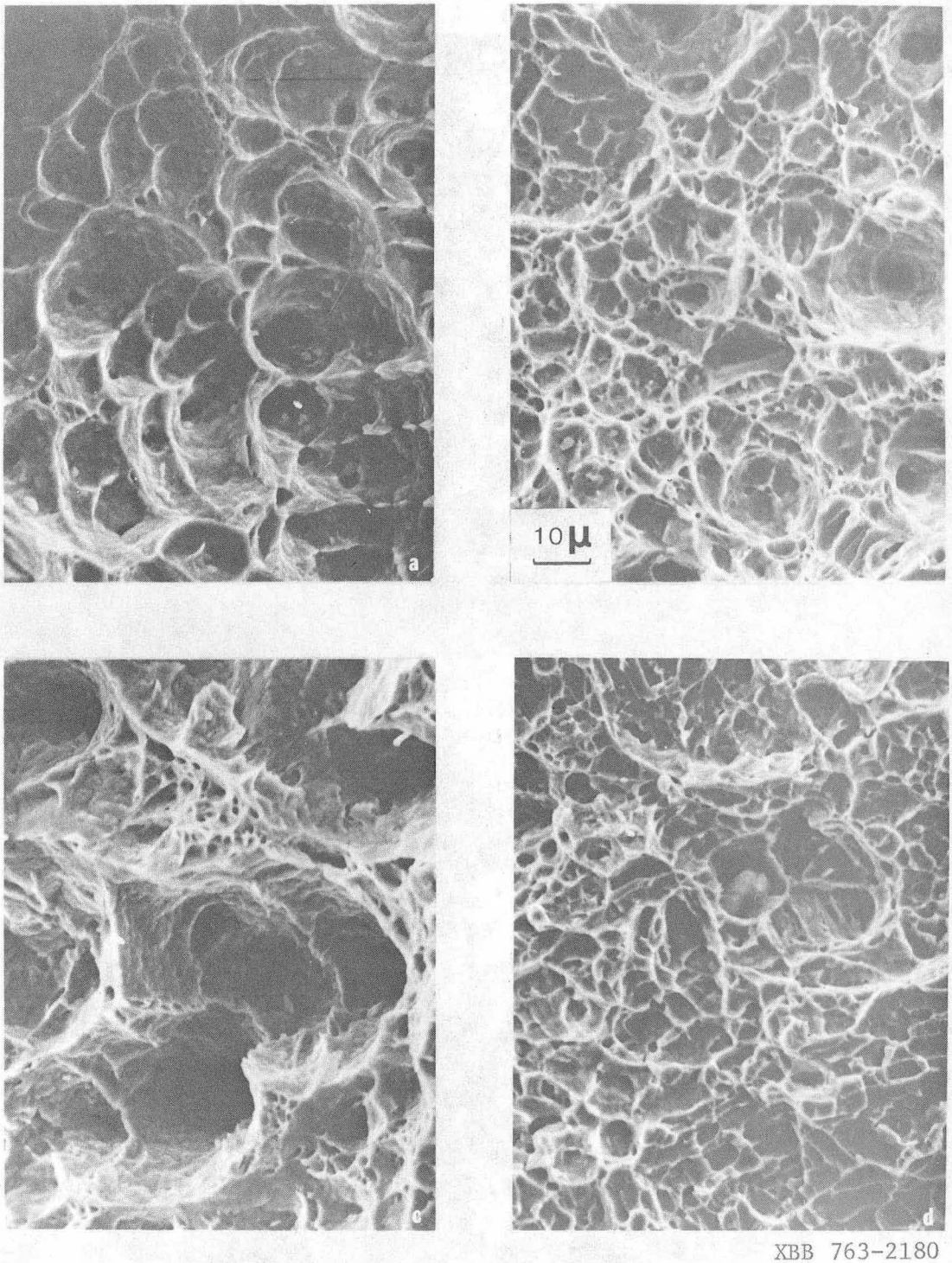

XBB 763-2180

Fig. 21.

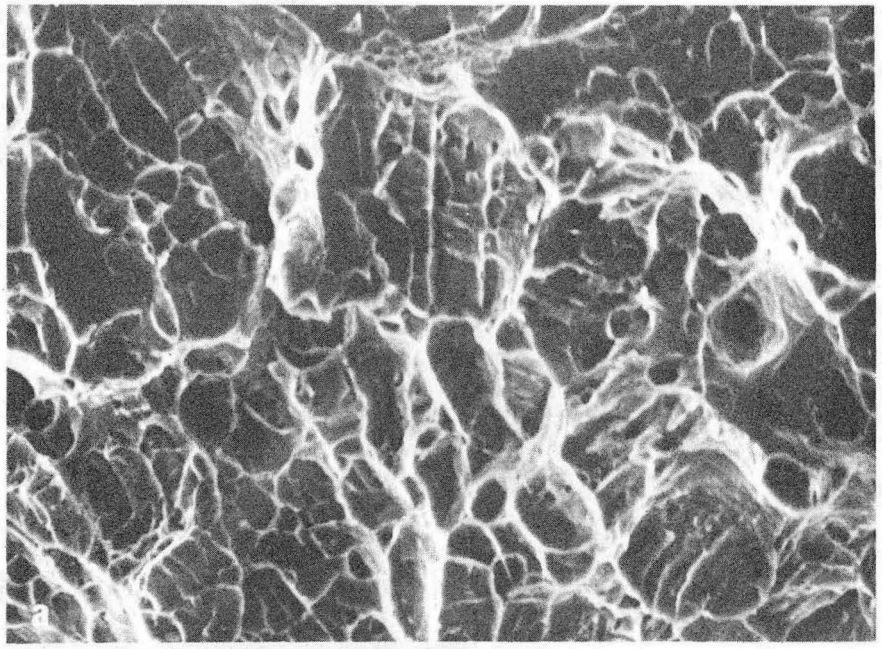

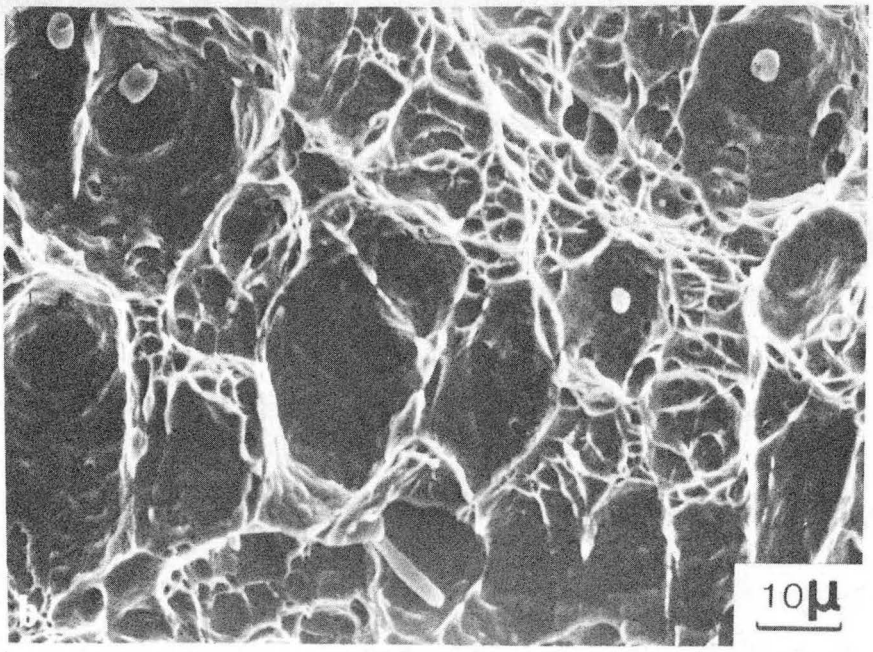

XBB 763-2176

Fig. 22.

TECHNICAL INFORMATION DIVISION
LAWRENCE BERKELEY LABORATORY
UNIVERSITY OF CALIFORNIA
BERKELEY, CALIFORNIA 94720